Title: Yet To Come…

A Dissertation Presented for the

Doctor of Philosophy

Degree

The University of Tennessee, Knoxville

Karl Jay Bernstein

December 2014

DEDICATION

Yada yada yada, my dedication.

ACKNOWLEDGEMENTS

Bla Blab la…

ABSTRACT

Garbly gook…

TABLE OF CONTENTS

Table of Contents

LIST OF FIGURES

INTRODUCTION

Statement of Purpose

Yadaydayday…

Literature Background

Asdfasdf

Raman Spectroscopy

The Raman phenomenon was first described by C.V. Raman and his student K.S. Krishna in 1928. The new scattering phenomenon, the fundamental process at heart of Raman Spectroscopy, was named for the discover and earned Raman a Nobel a few years later in 1930 demonstrating the impact of this discovery on science. Unlike the previously discovered Rayleigh scattering, Raman scattering is the inelastic scattering of light. The difference of energy can be a reduction or gain in net energy yielding Stokes and anti-Stokes scattering respectively. This difference in energy coincides with the loss or gain of energy from vibrational states of the interacting medium as illustrated with a Jablonski diagram in Figure 1.

Raman spectroscopy is usually performed using light in the visible range of the electromagnetic spectrum. However fluorescence often occurs in this range and generally overpowers Raman scattering in intensity. To alleviate issues arising from fluorescence experimenters often move further into the red where there is insufficient energy for the process. Raman scattering in general is a very weak process; for instance a typical absorption experiment will absorb 90 per cent of the incident light over a 1 cm path length, but only one in 10^{10} incident photons will undergo Raman scattering. This fundamental limitation is a challenge when using Raman spectroscopy. The classical depiction of Raman scattering is that a polarization is induced in a molecule by an oscillating electric field of incoming light. The induced dipole then radiates scattered light, without (Rayleigh) or with (Raman) exchanging energy with vibrations in the medium (e.g. molecule). The magnitude of the induced polarization, P, scales with the polarizability, α, and the incident electric field E:

$$P = \alpha E$$

Given this equation, the only methods to increase the magnitude of Raman scattering is to change the polarizability (e.g. your sample) or to raise the intensity of the electric field (e.g. light source).

Hyper-Raman Spectroscopy (HR)

Hyper-Raman scattering is the two photo form of Raman scattering, requiring that two photos scatter at the same time. The process was first documented in 1965 by Terhune, Maker, and Savage. While intensities, selection rules, and depolarization ratios for ordinary Raman are represented by the linear terms in the expansion of the dipole moment of a molecule; the description for hyper-Raman is represented mathematically by the first set of nonlinear terms in the equation:

$$P = \alpha E + \frac{1}{2}\beta E^2 + \cdots$$

The magnitude of the induced polarization, *P*, scales with the polarizability, α, and the incident electric field, *E*, for normal Raman and the second polarizability, the hyperpolarizability is represented by half β and the electric field, *E*, squared. The Raman activity of the analyte is determined by the polarizability and the Hyper-Raman activity is determined by the hyperpolarizability. Two researchers, Long and Stanton, explored hyperpolarizability in 1970 and found the polarizability to generally be a million times, six orders of magnitude, greater than the hyperpolarizability. A benefit of hyper-Raman is differing selection rules from either IR or Raman, meaning that inactive vibrational modes in IR and Raman may be observed in hyper-Raman.

Surface-Enhanced Raman Spectroscopy (SERS)

Raman scattering is a weak process that can lack sensitivity needed for many experiments. However, the physics behind Raman can dictate that the process be used for the specific work. Assuming that the sample (and the polarizability α) cannot be changed that leaves only the electric field E to be increased in order to get a stronger signal for more sensitivity, yet high electric fields result in photo bleaching and sample degradation. The answer to these challenges is often surface-enhanced Raman spectroscopy.

First observed and documented by Fleischmann, Hendra and McQuillan in 1974 SERS is a method which utilizes incredibly intense, localized electric fields while avoiding destroying the sample. While there is still some debate concerning the exact mechanism of SERS it is generally agreed that there is an electromagnetic enhancement aspect. The electromagnetic enhancement is derived for the excitation of localized surface plasmon resonance (LSPR), in essence, an "electron wave" that oscillates in resonance with incident electromagnetic fields. As the name indicates, LSPRs are highly localized only lending an enhancement near the surface they originated from, generally within two to ten nanometers. Hence, for SERS to be used the analyte must be on or very near the surface of an enhancing substrate. While the experimental constraints of SERS are substantial, the benefits are enormous with a typical enhancement of ten to 100 million times the signal (seven to eight orders of magnitude) and enhancements of 100 billion or more (11 orders of magnitude) reported. The enormous boost in intensity allows the experimenter to use much lower powers, for less time and still receive more signal than they would get with higher power and longer experiments. SERS also provides the benefit of quench competing fluorescence which can be of great benefit to experimenters.

Plasmoic Surfaces

SERS requires plasmoic surfaces to support LSPRs and provide an enhancement. Fleischmann et. al. initial work had used a silver electrochemically electrode. The electrode had been cycled numerous times which led to the surface becoming roughened or microscopically textured. This was important as it was the coarseness of the surface that permits the formation of LSPRs and SERS enhancement. While electrochemically roughened electrodes are rarely used today in SERS work the prerequisite of a microscopically textured surface is still key to the substrates used in all SERS work. The fact that the electrode was silver also turns out to be important as the LSRPs of silver and gold typically resonate within the visible spectrum of light. Most SERS active substrates are consist of either gold or silver.

One popular SERS substrate is colloidal aggregates. Colloids are chemically synthesized, typically from silver or gold, in the laboratory as a colloidal suspension. A sample is introduced to the suspension where it must then migrate to the surface of the colloids. While still a colloidal suspension very little if any enhancement will be observed. Then either the sample will cause the colloids to aggregate and crash out of solution, collecting at the bottom of the container or a salt will be added to induce the crash out. When the colloids collect in an aggregate, the spheroid particles end up touching or nearly touching and it is at these junctions between particles that LSPRs are excited and provide the SERS enhancement.

Another popular substrate are thin island films. Named for the thin amount of material present in island like patches these films are often made using physical vapor deposition. This process vaporizes small amounts of, typically silver or gold, metal and deposits it onto a substrate such as glass. Only a very thin layer around ten nanometers is typically used. The

process creates a rough surface of island like collections of the metal that provide the texture necessary for LSPR formation and SERS enhancement.

A modification of thin island films are film over nanospheres or FONs. In this case small spheres, usually 100 to 500 nm in diameter are deposited in a monolayer on a substrate. Then a much thicker layer of metal, typically 100 to 200 nm is deposited on top of the spheres. The metal deposited on FONs ends up being highly textured and multiple junctions between spheres provide ample locations for LSPR excitement and SERS enhancement. The greater bulk of material and thickness of metal used for FONs make the SERS substrate much more robust than thin island films.

CHAPTER SUMMARIES

Blab la.

INTRODUCTION REFERENCES

Text.

CHAPTER I.

SERS STUDY OF PHOSPHINES AND PHOSPHINE OXIDES ON SILVER

Rational For Phosphine Surface Experiment

Organic group (R-groups) binding to metals typically occur in either a Lewis acid/base type adduct or in a covalent manner, known respectively as an L-type or X-type bond as proposed by Green et al. Aryl thiols have been used widely to create monolayers on metal surfaces and are known to bind by the loss of a proton to create robust covalent bonds with the metal surface. Phosphorus directly neighbors sulfur on the periodic table and would be expected to have similar chemistry. Yet the bonding motif of aryl phosphines has yet to be explored. Phosphines are widely used in synthetic and catalytic processes which are used extensively in industrial applications. Briefly describe an industrial application of phosphines. Phosphines also find specialized use as highly chiral selective reagents for pharmaceuticals. Briefly describe pharma use. A better understanding of how phosphines bind to metals should improve our ability to use them. I began an/An investigation of phosphorus-metal bonds by examining the binding of a select group of tertiary phosphines, secondary aryl phosphines and secondary aryl phosphine oxides, illustrated in Figure 1.1-2, with SERS.

These specific phosphines were chosen for the select ways in which they can bind. Tertiary phosphines are covalent-bond saturated and may only bind via a L-type bond using lone pairs. The secondary phosphines may bind with either lone pairs for an L-type bond or by losing the proton for an X-type bond. The secondary phosphine oxide may bind via an L-type bond only using one of the oxygen's lone pair or by again losing a proton and forming a X-type bond. By investigating the selected phosphines with a surface specific technique such as SERS to determine which bind to a metal surface will, process of elimination, allow for a determination of the binding method.

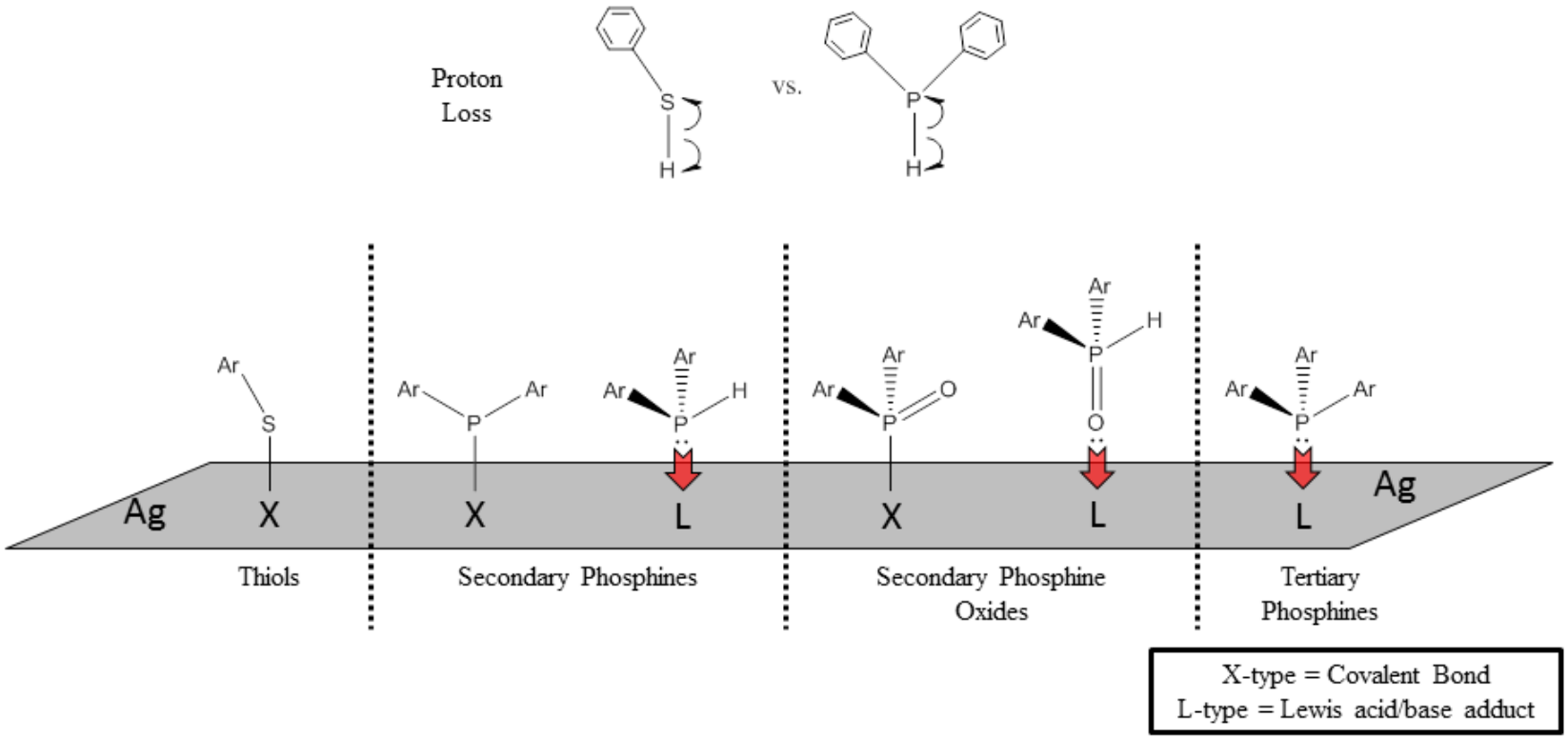

Figure 1.1. A schematic representation of the bonding mode of aryl thiols on a silver surface vs. the potential bonding modes of secondary phosphines, secondary phosphine oxides, and tertiary phosphines.

Tertiary Phosphines

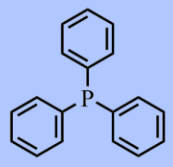

Triphenylphosphine (Tpp)
Formula: C18 H15 P
Cas: 603-35-0
MW: 262.29

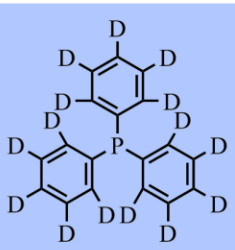

Tri(phenyl-2,3,4,5,6-d5)-Phosphine (Tppd15)
Formula: C18 D15 P
Cas: 24762-44-5
MW: 277.38

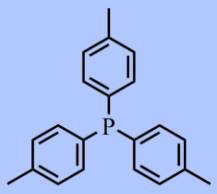

Tris(4-methylphenyl)-phosphine (T4mpp)
Formula: C21 H21 P
Cas: 1038-95-5
MW: 304.371

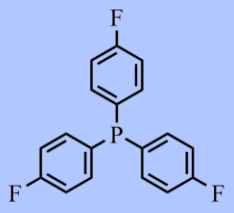

Tris(4-fluorophenyl)-phosphine (T4fpp)
Formula: C18 H12 F3 P
Cas: 18437-78-0
MW: 316.261

Secondary Phosphines

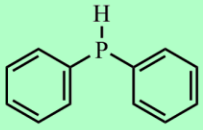

Diphenylphosphine (Dpp)
Formula: C12 H11 P
Cas: 829-85-6
MW: 186.189501

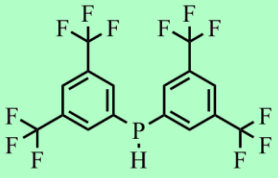

Bis[3,5-bis(trifluoromethyl)phenyl]-phosphine (Btfpp)
Formula: C16 H7 F12 P
Cas: 166172-69-6
MW: 458.18

Secondary Phosphine Oxides

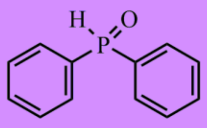

Diphenylphosphine oxide (Dppo)
Formula: C12 H11 O P
Cas: 4559-70-0
MW: 202.1889

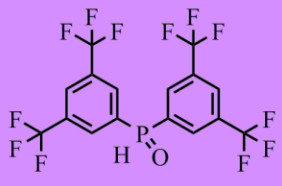

Bis[3,5-bis(trifluoromethyl)phenyl]-phosphine oxide (Btfppo)
Formula: C16 H7 F12 O P
Cas: 15979-14-3
MW: 474.18

Figure 1.2 Selection of Phosphines for studies.

Experimental Limitations

Initial experiments were performed with normal Raman, spectra were recorded from crystalline material without issue. The tertiary phosphines used were triphenylphosphine (tpp), triphenylphosphine d-15 (tppd15), tris(4-methylphenyl)-phosphine (t4mpp), and tris(4-fluorophenyl)-phosphine (t4fpp). Then, to record SERS spectra the silver colloidal solution method was chosen. To begin with Lee and Meisel's method was used to fabricate the silver colloids; this colloidal synthesis, as most are, was performed in aqueous solution. Phosphines typically have a very low affinity for water however and are practically insoluble. To combat this issue the colloids were resuspended in ethanol by centrifuging the aqueous suspension, decanting the aqueous supernatant and resolvating in alcohol. Within a few hours of incubation with the phosphines, the colloidal solution would begin to clear and no SERS activity was observed. A different colloid synthesis by Leopold and Lendl was then used, that were also resuspended in alcohol, which would crash out with phosphine concentrations in the millimolar range or less after 12 hours of incubation. Colloid solutions with less than micromolar concentrations of phosphines failed to crash out. This second colloidal fabrication technique yields particles with a greater size distribution than the synthesis of Lee et al and it was believed that this greater distribution of sizes is what led to the colloids working.

Results and Discussion

The Raman spectrums of tpp, tppd15, t4mpp and t4fpp share several spectral features, displayed in Figure 1.3 with a few differences. The incredibly intense benzene breathing mode is a dominant feature in all four spectra, for tpp this mode is located at 1000 relative cm^{-1}, for tppd15 at 960 rel cm^{-1}, for t4mpp and t4fpp at 1100 rel cm^{-1}. Another very characteristic peak for

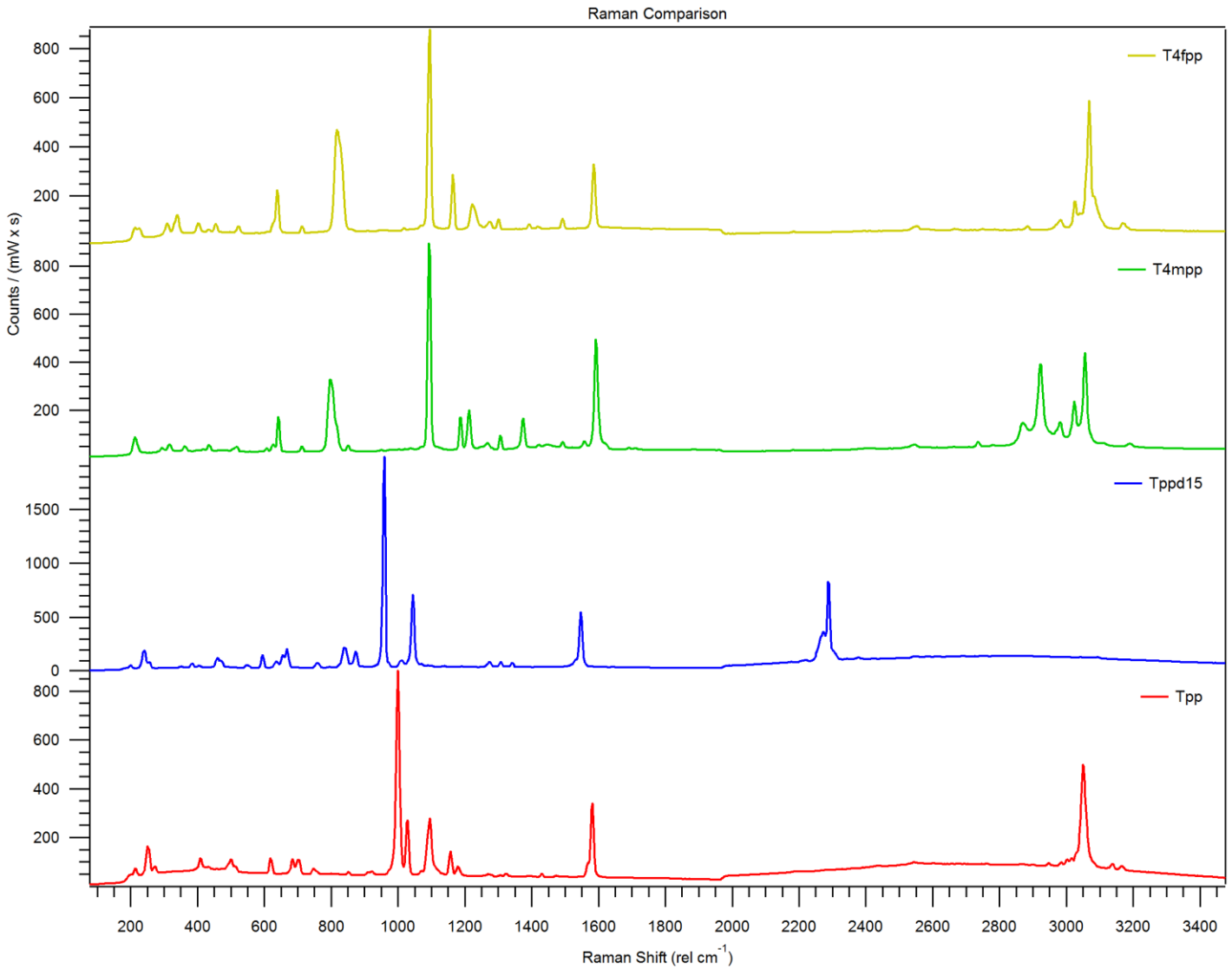

Figure 1.3. The Raman spectrums of tpp, tppd15, t4mpp, t4fpp.

all the compounds were the C-H stretches from the benzene rings at 3050, 2290, 3050, 3050 rel cm-1 for the four respective compounds. Tppd15 has a much lower value given that it has deuterium as opposed to typical hydrogen. **(Comment on peaks at ~1.6k and then 800 t4s).** Of special note on t4mpp, with the methyl groups off the para position of the aromatic rings shows a "trident" like set of peaks at 2870, 2920, 2980 rel cm^{-1} with the central peak being the most intense. Note, the dip at roughly 1970 rel cm^{-1} is an artifact from the experimental procedure and not an aspect of the spectrum.

When comparing the normal Raman spectrum to the SERS spectrum of tpp in Figure 1.4, we must first note that the presence of solvent contributions to the SERS spectrum which are denoted with a star or asterisk (*). Other than these additions the two spectra correspond quite closely. The benzene breathing modes, C-H stretches, and several of the other rather intense peaks match up closely confirming that tpp was observed in the SERS spectrum. Furthermore, the normal Raman spectrum was recorded from a crystal over twenty five seconds with 6.45 mW of laser power while the SERS spectrum was taken of a milimolar concentration tpp solution over twenty five seconds at 588 uW of laser power. An order of magnitude less laser power and several orders of magnitude lower concentration while getting more than an order of magnitude more signal demonstrates that an enhancement is occurring and that this is indeed a SERS spectrum.

Examining the comparison plots for tppd15, t4mpp and t4fpp in Figures 1.5-7 the same trends repeat, the benzene breathing modes, C-H stretches and several of the other intense peaks match up nearly exactly. Of special note in t4mpp is the incredibly intense "trident" like set of peaks. This is due to the methyl group on the para position of the benzene rings and the ethanol solvent overlapping, making these peaks much more intense than they otherwise would be.

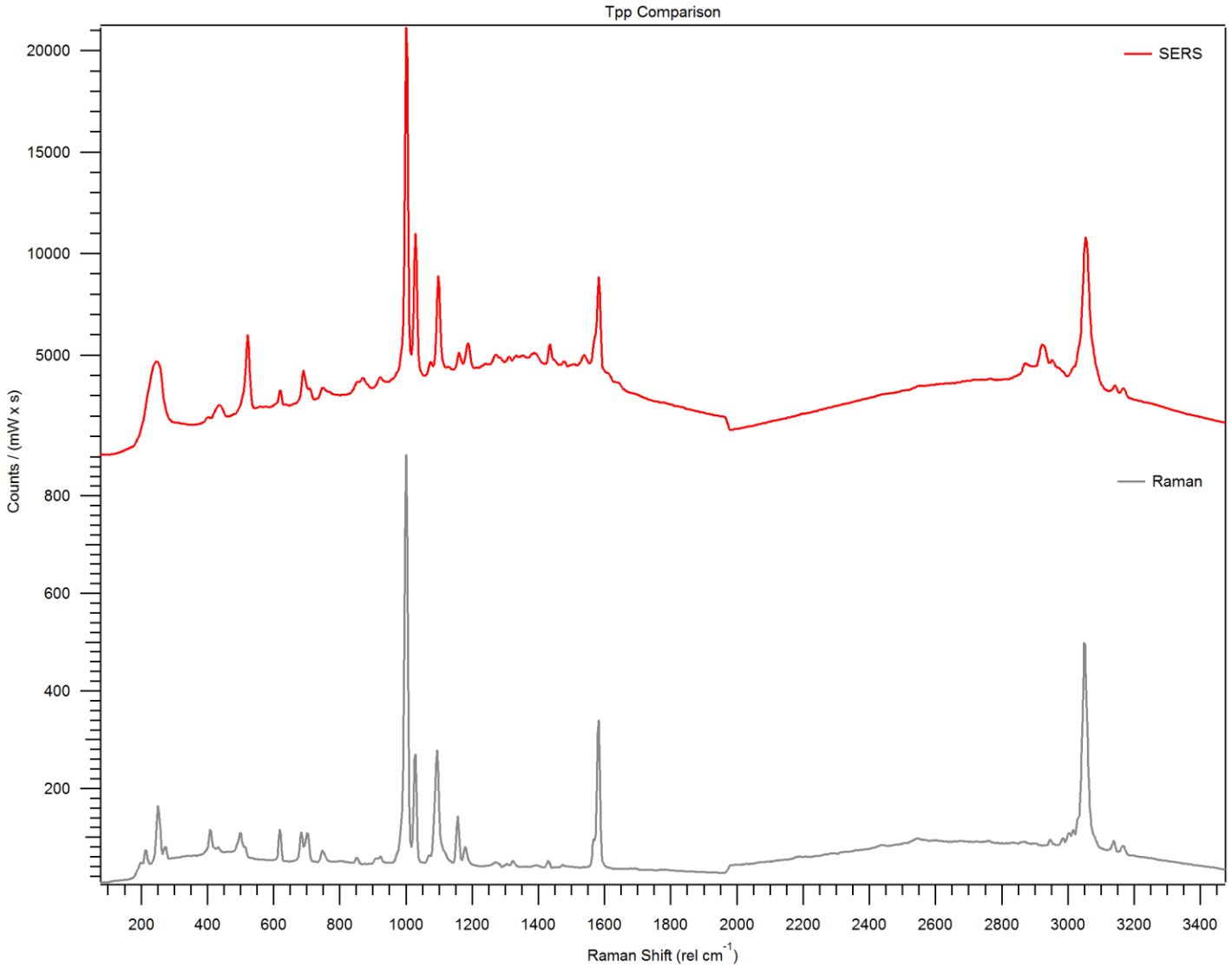

Figure 1.4. SERS spectrum of Tpp top and normal Raman spectrum bottom.

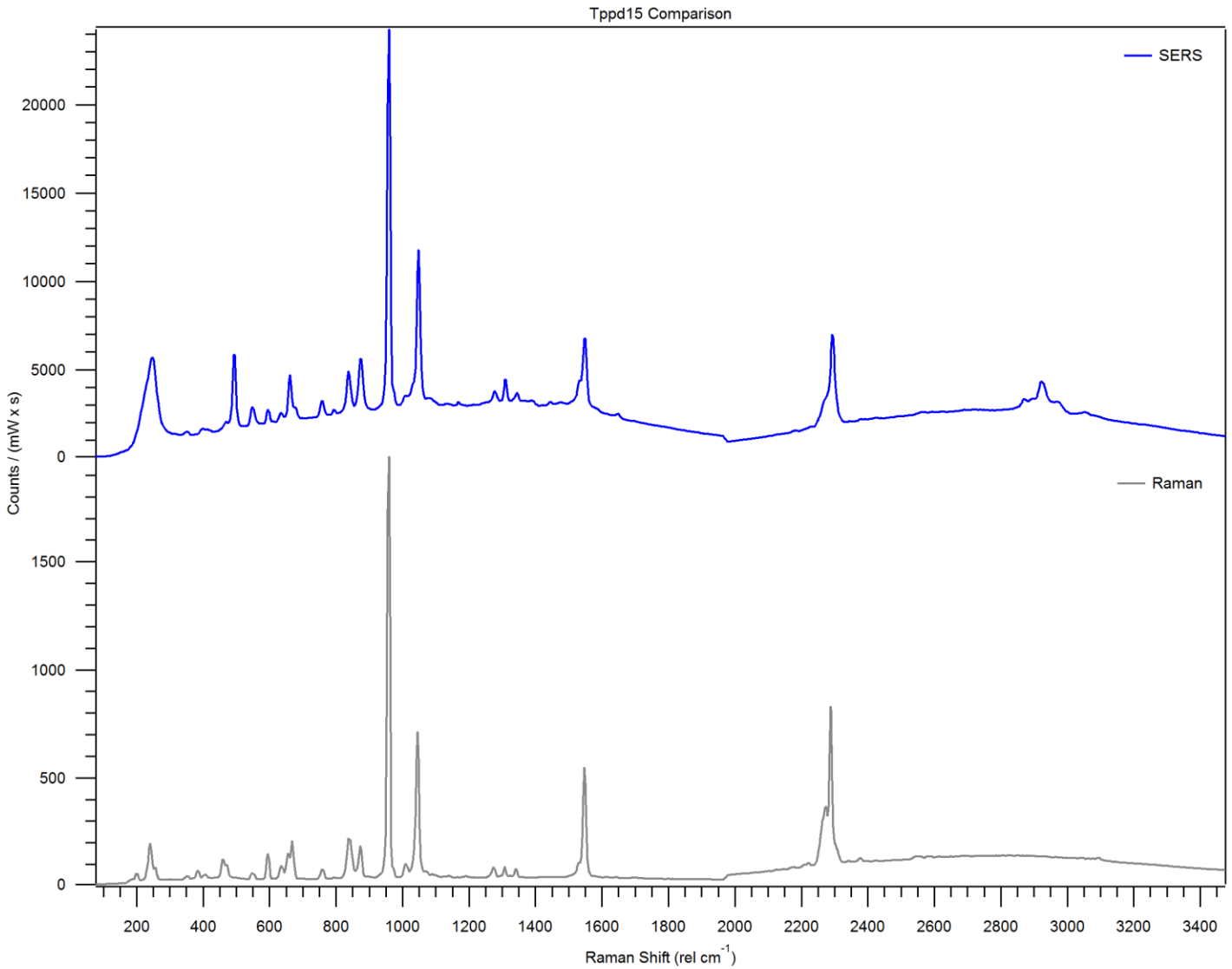

Figure 1.5. SERS spectrum of Tppd15 top and normal Raman spectrum bottom.

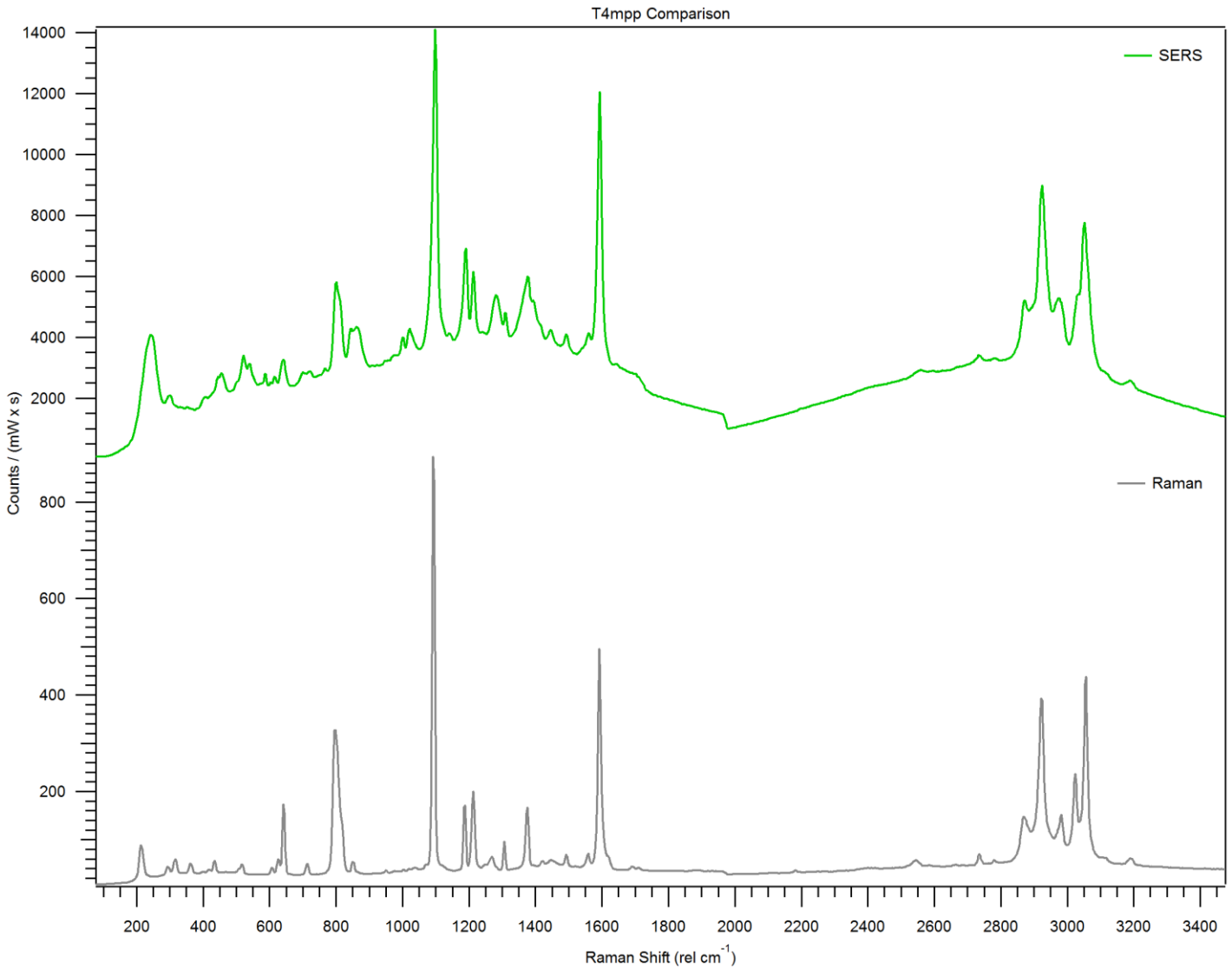

Figure 1.6 SERS spectrum of T4mpp top and normal Raman spectrum bottom.

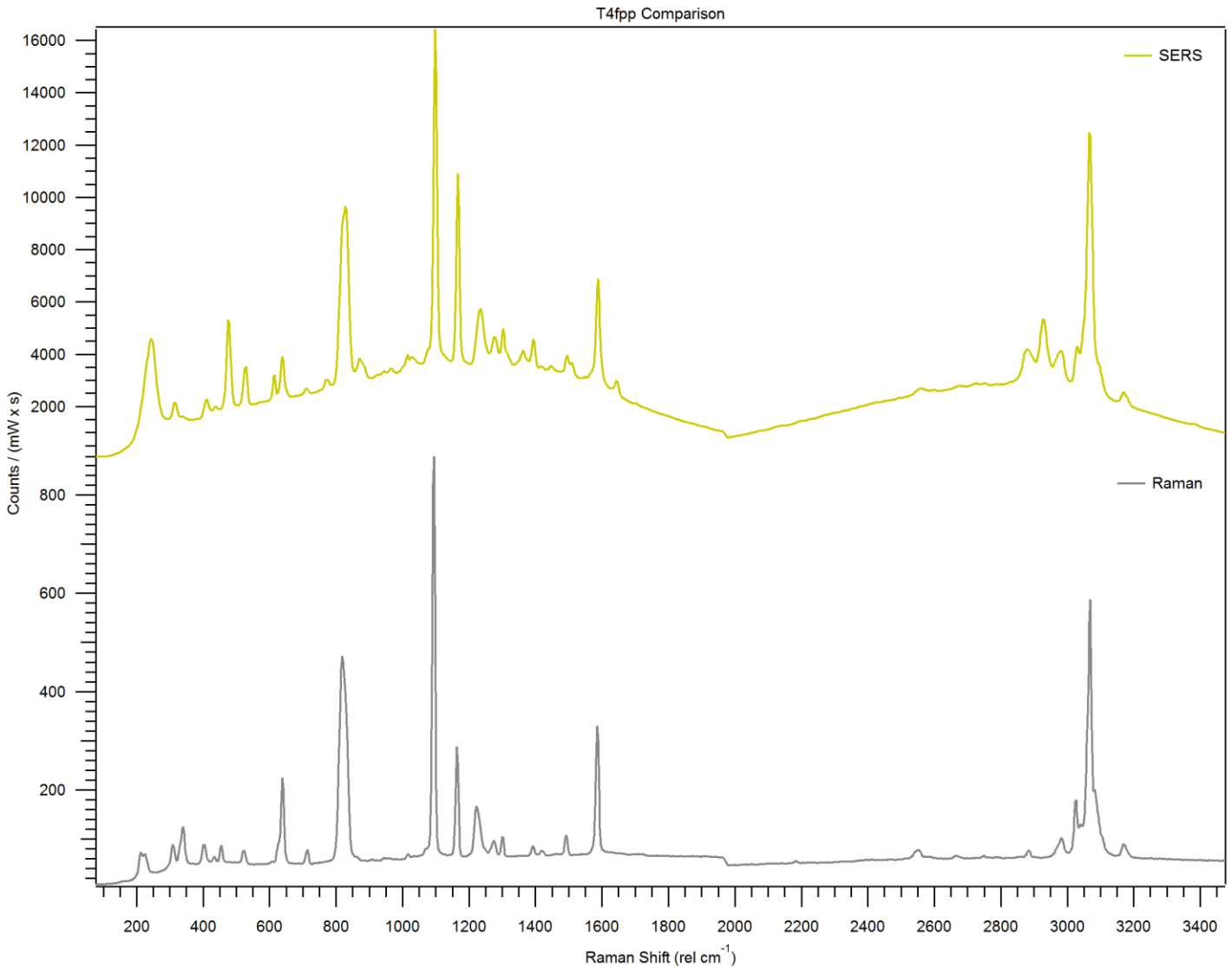

Figure 1.7 SERS spectrum of T4fpp top and normal Raman spectrum bottom.

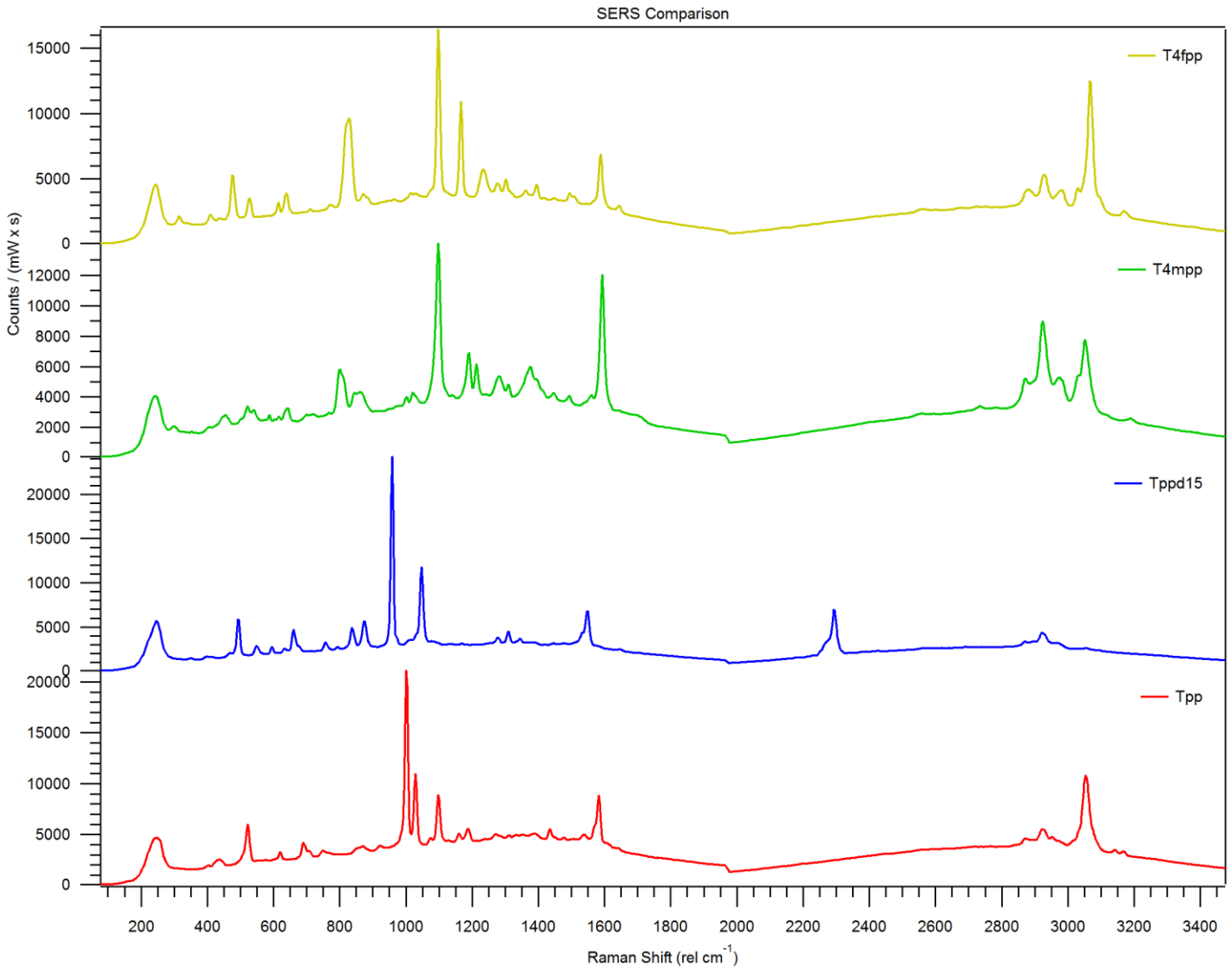

Figure 1.8 SERS spectra of all four tertiary phosphines, Tpp on the bottom and going up, Tppd15, T4mpp and T4fpp at the top. Contributions from solvent marked with an asterisk (*).

This phase of experimenting has verified that we've gotten SERS spectra of the four tertiary phosphines. Given that SERS spectra have been confirmed for all four tertiary phosphines as shown again in Figure 1.8 and there is not a proton present to be lost we can confirm that L-type bonding must be the method of binding. This is the first of three test in the series of experiments to be performed with the phosphines.

Tests were then run with the secondary phosphine oxide, diphenylphosphine oxide (Dppo), in colloids. Unlike the triphenylphosphines, the colloids when incubated with Dppo failed to crash out at the same concentrations and when salts were added to force the crash out no activity from Dppo was observed as shown in Figure 1.9. While several modes are clearly visible in the plot labeled SERS, this is not SERS from the analyte, but from the capping agent and other compounds from the colloids. The benzene breathing mode is not present, the C-H stretch is at the wrong frequency, the mode at 2400 rel cm^{-1} is completely absent as is the peak at 700 and 1600. Furthermore the peaks in the 800-1400 rel cm^{-1} range do not match up. Thus we are not seeing SERS activity from the analyte. Given that we are not seeing binding of Dppo, or a secondary phosphine oxide we have ruled out the binding modes for the oxides, the second of three tests in the series.

Films For Oxygen Free Environment

The secondary phosphines, diphenylphosphine (dpp) and Bis[3,5-bis(trifluoromethyl)phenyl]-phosphine (Btfpp), can be oxidized by atmospheric oxygen, thus all initial Raman measurements were made in sealed containers under inert atmosphere. To carry out SERS experiments though, where even a small amount of impurity could show up in an overwhelming majority due to the selective enhancement, a different substrate than the colloidal

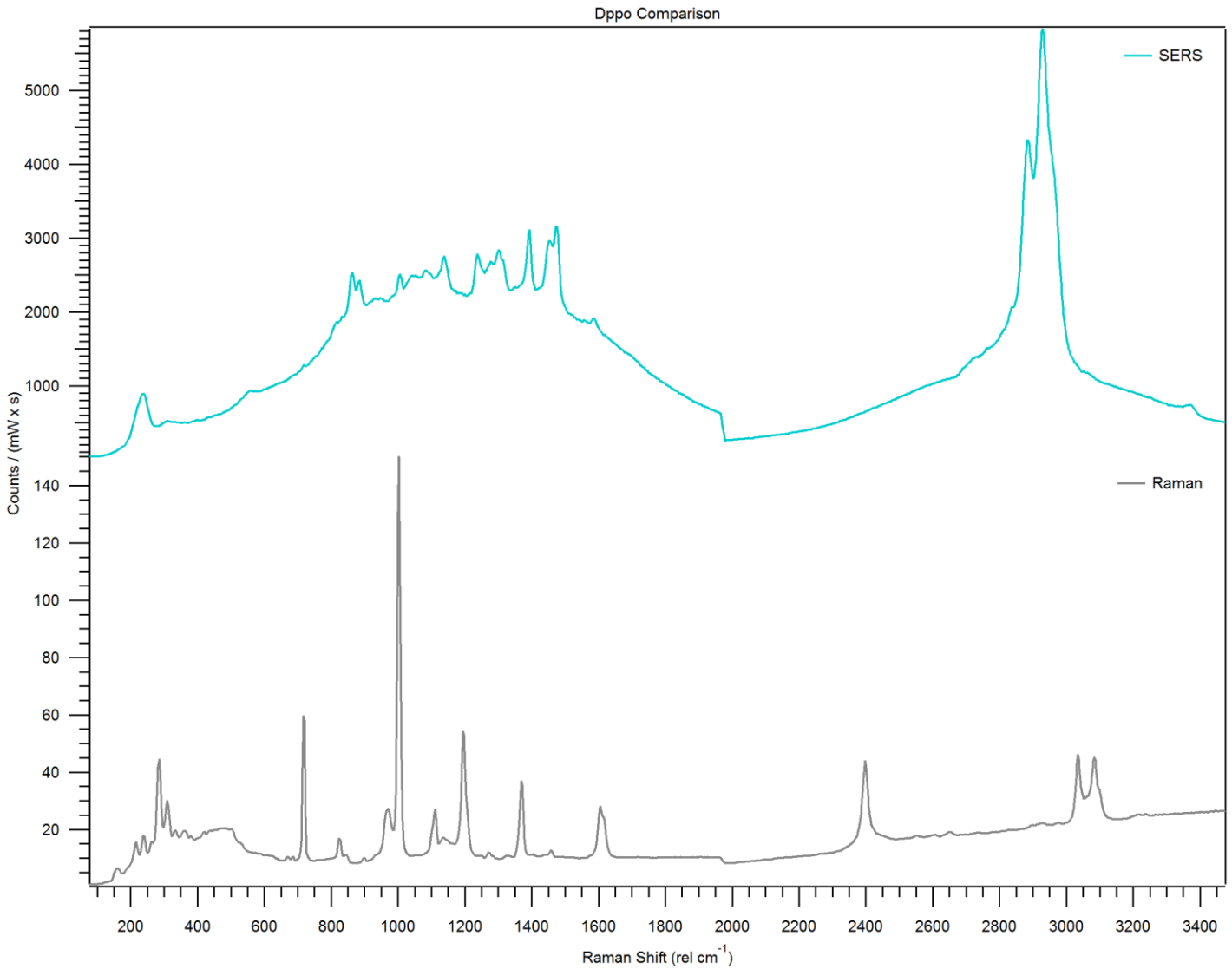

Figure 1.9 The attempted SERS spectrum of Dppo top and normal Raman spectrum bottom.

suspensions would be required in order to have an oxygen free test. A suitable alternative of silver island films (SIFs) were chosen. The thin films were a solid metal substrate that could be pumped under a vacuum or put under inert atmosphere without harm unlike aqueous solution suspended colloids. The films were first tested with the tertiary phosphines to establish experimental parameters. It was found that the phosphines completely strip the silver from the glass substrate even at very low concentrations. Several different exposures were tested but all resulted in the stripping of the film. Thus the SIFs would not work and the final experiment in the series of three could not be completed.

Until a method to test the secondary phosphines in an oxygen free atmosphere can be utilized and the experiment run, this series of experiments will ultimately be inconclusive. The experiments that were completed indicate that phosphines bind in an L-type method exclusively (see Figure 1.10). This was the type of binding that was observed with the tertiary phosphines and the method unavailable to the secondary phosphine oxide.

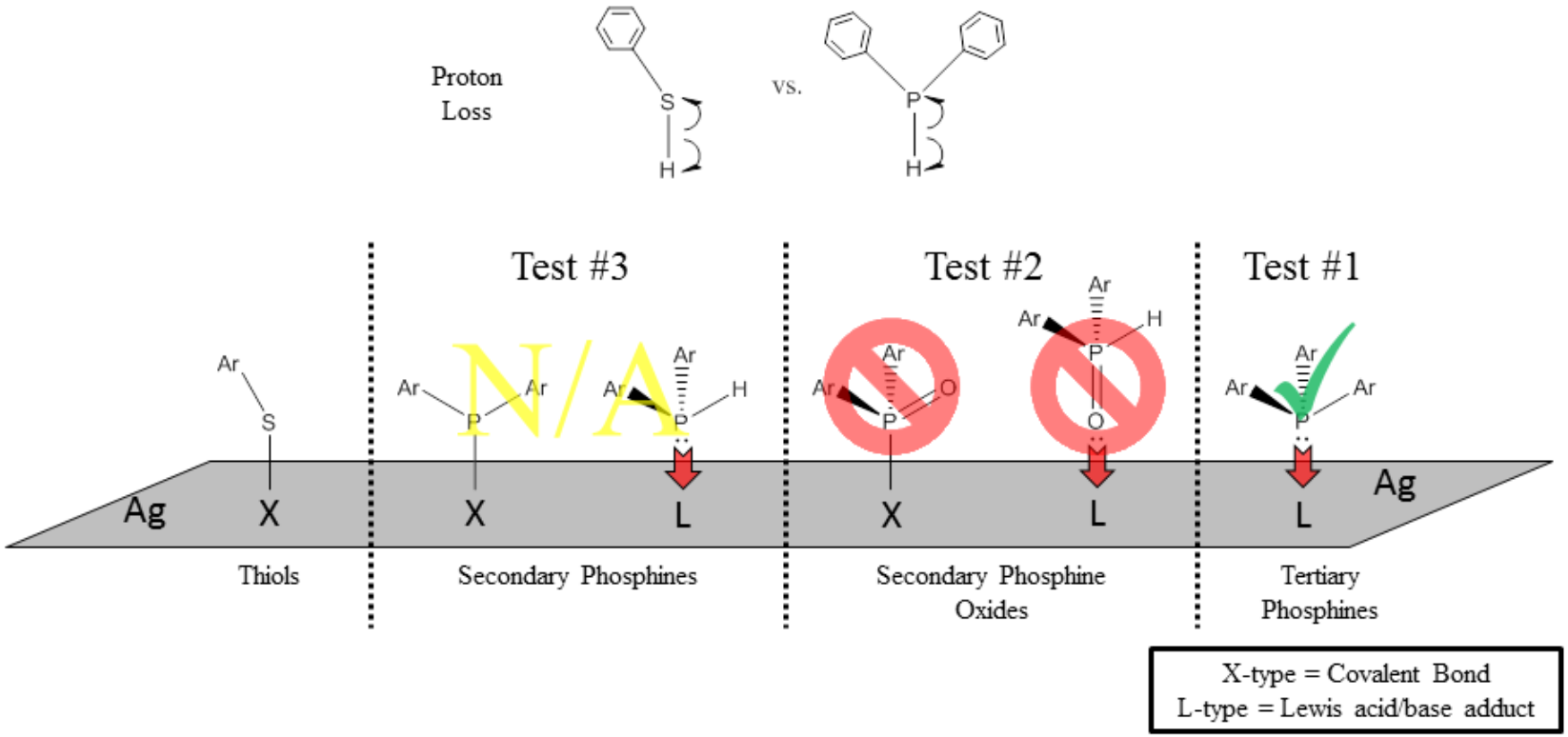

Figure 1.10 A schematic representation of the outcome of bonding mode of aryl thiols on a silver surface vs. the potential bonding modes of secondary phosphines, secondary phosphine oxides, and tertiary phosphines. Test #1 demonstrated a L-type binding motif while Test #2 proved the phosphine would not bind in an X-type motif losing a proton or an L-type motif through they Oxygen present. Test #3 could not be performed due to experimental difficulties.

CHAPTER II

THE SYNTHESIS AND SPECTROSCOPIC CHARACTERIZATION OF AN AROMATIC URANIUM AMIDOXIME COMPLEX

A version of this chapter was originally published by Karl J Bernstein, Chi-Linh Do-Thanh, Deborah A. Penchoff, S. Alan Cramer, Christopher R. Murdock, Zheng Lu, Robert J. Harrison, Jon P. Camden and David M. Jenkins:

Bernstein, K. J., Do-Thanh, C., Penchoff, D. A., Cramer, S. A., Murdock, C. R., Lu, Z., Harrison, R. J., Camden, J. P., and Jenkins, D. M. **THE SYNTHESIS AND SPECTROSCOPIC CHARACTERIZATION OF AN AROMATIC URANIUM AMIDOXIME COMPLEX.** *Inorganica Chimica Acta* (2014), 421, 374-379.

The article is represented in the published form, with the exception that the following Inorganica Chimica Acta sections have been removed: Article history, Keywords, acknowledgements. The Supporting Information section of the manuscript has been added as an appendix. The dissertation author was involved in full breath of this work, participating in all experimentation, data analysis, and performed the vibrational spectroscopy. The 1,8-naphthalimide dioxime, **3**, (Np-CAO-H3) molecule was synthesized by C. Do-Thanh, Mass spectroscopy and 2D NMR were led by S. A. Cramer, solid state NMR were led by C. R. Murdock, single crystal X-ray analysis and structure deconvolution was performed by Z. Lu, these four individuals were under the guidance of D. M. Jenkins. DFT calculations and analysis were performed by D. A. Penchoff under the guidance of R. J. Harrison. All authors participated in the discussion of results and approved the final manuscript.

Abstract

A tridentate aromatic amidoxime ligand and its corresponding uranyl complex have been synthesized. The complex was rigorously characterized with single-crystal X-ray diffraction,

solid-state NMR, infrared absorption, and Raman spectroscopy. Unlike previous amidoxime complexes, the crystal structure confirms the complexation of only a single tridentate amidoxime ligand to the uranium, and solid state NMR confirms uranyl binding in the bulk sample. The Raman spectrum of the complex is dominated by the strong U═O vibration which exhibits a significant shift from the U═O vibration in unbound uranyl. Density functional theory (DFT) aided in calculations of vibrational modes as well as providing insight into the electronic structure of this uranyl complex.

Published Work

Introduction

Aqueous uranyl chemistry is experiencing a renaissance due to two distinct, but related, applications: extraction of uranium from seawater and nuclear forensics [1–4]. Due to the very low concentration of uranium for each application, sorption methods are considered the only viable option as a result of financial and environmental considerations [5,6]. The oceans contain the uranyl ion at an uniform concentration of 3.3 ppb (ppb) [7,8]; this ubiquity of uranium in nature and its destructive potential as a weapon underpin the necessity of nuclear forensics. This field is concerned with who has harnessed uranium's deadly capabilities and it has typically relied heavily on lab-based mass spectrometry for analysis [2,9]. Uranyl extraction from seawater and spectroscopic detection for nuclear forensics could benefit from the development of highly selective uranyl binding ligands. Several complexing agents for sorptive methods of uranyl extraction have been investigated, and evaluated based on selectivity, robustness, loading capacity, and rate of uptake [5,10–13]. After extensive methodology evaluation, amidoxime

functionalized polymers were selected as optimal [5]. Further investigation of the uranyl complexing polymers revealed the presence of cyclic, polydentate amidoximes alongside the normal amidoximes [10]. Recent advances in understanding the binding of polydentate amidoximes to uranyl by Hay [14] and Rao [15–17] provided insight into the structural motifs that are possible when employing these ambidentate ligands. While simple amidoximes have been well characterized by a variety of spectroscopic techniques, their cyclic counterparts have received far less attention [18]. To our knowledge, detailed spectroscopic measurements, such as NMR, IR, and Raman, have not been collected on any of the cyclic amidoxime uranyl complexes. Vibrational spectroscopy is of particular interest since these initial measurements would be necessary to determine if these systems could be viable in the field of nuclear forensics. In this manuscript, we describe the synthesis of a tridentate amidoxime ligand that complexes with uranyl in a 1:1 fashion. The uranyl complex was structurally characterized by single crystal X-ray diffraction. In addition to the structural characterization, additional solid state spectroscopic methods such as NMR, IR, and Raman were employed. The Raman spectroscopy suggests that conjugated ligands like this one could lead to novel detection methods for actinides.

Experimental

Materials

The compound acenaphtho[1,2-c][1,2,5]thiadiazole 8,8-dioxide (1) was prepared via a modification of the published procedure of Qian [19]. Compound **1** was also prepared by Wright [20]. 1,8-dicyanonaphthalene (**2**) was synthesized in a manner similar to Ege's pyrolysis

approach (Ege provided no characterization of the product except melting point) [21]. 1,8-naphthalimide dioxime (**3**) was prepared via adaptation of the published procedures of Forrester [22]. Our detailed synthetic procedures and analytical data are described below. All other reagents were purchased from commercial vendors and used without further purifications.

Methods and instrumentation

^{1}H and $^{13}C\{^{1}H\}$ solution spectra were recorded at ambient temperature on a Varian VNMRS 500 MHz narrow-bore system. ^{1}H, $^{13}C\{^{1}H\}$, HSQC, and HMBC NMR chemical shifts were referenced to the residual solvent. Solid ^{13}C CP MAS NMR samples were recorded on a Varian Inova 400 MHz spectrometer and referenced to an external adamantane sample. ^{13}C CP MAS with interrupted decoupling (to suppress protonated carbons) was applied using a spin rate of 6 kHz with the dipolar dephasing turned on for 100 μs. All mass spectrometry analyses were conducted at the Mass Spectrometry Center located in the Department of Chemistry at the University of Tennessee. The DART analyses were performed using a JEOL AccuTOF-D time-of flight (TOF) mass spectrometer with a DART (direct analysis in real time) ionization source from JEOL USA, Inc. (Peabody, MA). The ESI/MS analyses were performed using a QSTAR Elite quadrupole time-of-flight (QTOF) mass spectrometer with an electrospray ionization source from AB Sciex (Concord, Ontario, Canada). Sample solutions of complexes for mass spectrometry were prepared in acetonitrile, tetrahydrofuran, or DMSO (for uranium complex, **4**, only). Carbon, hydrogen, and nitrogen analyses were obtained from Atlantic Microlab, Norcross, GA.

X-ray structure determination

Data was collected on a Bruker SMART APEX II three circle diffractometer equipped with a CCD area detector and operated at 1800W power (45 kV, 40 mA) to generate Mo Kα radiation (λ = 0.71073 Å). The incident X-ray beam was focused and monochromated using Bruker Excalibur focusing optics. Single crystals were mounted on nylon CryoLoops (Hampton Research) with Paratone-N (Hampton Research) and frozen at -173 °C. Initial scans of each specimen were taken to obtain preliminary unit cell parameters and to assess the mosaicity (i.e. breadth of spots between frames) of the crystal to select the required frame width for data collection. For all cases frame widths of 0.5° were judged to be appropriate and full hemispheres of data were collected using the BRUKER APEX2 software suite to carry out overlapping φ and ω scans at detector setting of $2\theta = 28°$. Following data collection, reflections were sampled from all regions of the Ewald sphere to re-determine unit cell parameters for data integration. Following exhaustive review of collected frames the resolution of the dataset was judged, and, if necessary, regions of the frames where no coherent scattering was observed were removed from consideration for data integration using the BRUKER SAINTPLUS program [23]. Data was integrated using a narrow frame algorithm and was subsequently corrected for absorption. Absorption corrections were performed for both samples using the SADABS program [23]. Space group determination and tests for merohedral twinning were carried out using XPREP [23]. In all cases, the highest possible space group was chosen. Final models were refined anisotropically (with the exception of H atoms). The *Addsym* subroutine of PLATON [24] was utilized to assure that no additional symmetry could be applied to the models.

Vibrational spectroscopy

Excitation was provided by a HeNe laser (HNL100L, Thorlabs) with a laser line of 632.8 nm and a power of 0.6 mW at the objective. An inverted microscope (Ti-U, Nikon Eclipse) with

a 10x, 0.30 NA dry objective (Nikon) in the 180° configuration was used in conjunction with Rayleigh filter and dichroic (Semrock) to collect the Raman scattering. Spectra were recorded with a 300 cm focal length spectrometer (Acton, Princeton Instruments) containing a 1200 groove mm^{-1} holographic grating, and a 10 μm slit with an attached liquid-nitrogen-cooled deep-depletion charge-coupled device (CCD, Spec10, Princeton Instruments). Spectra were calibrated with cyclohexane. Infrared spectra were collected on a Thermo Scientific Nicolet iS10 with a Smart iTR accessory for attenuated total reflectance. Raman and IR spectra were both obtained from the crystalline solid.

Computational methodology

Geometry optimizations and vibrational frequencies were obtained with the NWCHEM [25] package using density functional theory (DFT), and the B3LYP functional [26–28]. The Stuttgart RSC 1997 effective core potential and its corresponding basis set was used for uranium [29] (with the most diffuse S, P, D, and F functions removed, i.e., those with exponent 0.005, since they pertain only to the neutral metal atom and cause numerical problems in molecules), and the 6-311++g** basis set was used for oxygen, nitrogen, carbon, and hydrogen atoms [30]. The ECP accounts for relativistic effects and replaces 60 electrons of uranium with a pseudopotential. Basis sets were obtained from the EMSL database [31,32]. This computational protocol has been established as producing reliable geometries and energetics for uranyl complexes [33]. Geometry optimizations were performed with tight convergence settings. Frequency calculations were performed to obtain thermochemical corrections, and to verify that the structures reflect local minima. Volumetric data was generated with NWCHEM, modeled with Visual Molecular Dynamics (VMD) [34] and plotted with Persistence of Vision Raytracer (Pov-Ray) [35].

Synthesis of acenaphtho[1,2-c][1,2,5]thiadiazole 8,8-dioxide, 1

Sulfamide (15.8 g, 161 mmol) and *p*-toluenesulfonic acid monohydrate (1.36 g, 7.14 mmol) were added to acenaphthenequinone (10.0 g, 53.8 mmol) in absolute ethanol (400 mL), and the mixture was heated at 80 °C for 3 days. After cooling to room temperature, the solvent was removed by rotary evaporation. The residue was then extracted with methylene chloride (2 x 350 mL) from water (350 mL), and a light brown precipitate formed above the organic layer. The precipitate was collected, and the combined organic layers were dried with magnesium sulfate, filtered, and concentrated. The concentrate was combined with the precipitate and recrystallized from boiling pyridine (200 mL) to give the product as a light brown powder (7.35 g, 56.4% yield).

^{1}H NMR (DMSO-d_6, 499.74 MHz): δ 8.49 (d, J = 7.8 Hz, 2H), 8.45 (d, J = 7.8 Hz, 2H), 8.01 (t, J = 7.7 Hz, 2H). ^{13}C NMR (DMSO-d_6, 125.67 MHz): δ 166.24, 148.57, 133.26, 130.77, 129.71, 126.80, 123.13. IR (neat): 1630, 1581, 1485, 1415, 1355, 1170, 1091, 1070, 1038, 986, 942, 920, 831, 776, 738, 694, 663 cm^{-1}. HRDART/ MS (*m/z*): $[M+H]^+$ 243.0219 (found); $C_{12}H_7N_2O_2S$ 243.0228 (calcd).

Synthesis of 1,8-dicyanonaphthalene, 2

Acenaphtho[1,2-c][1,2,5]thiadiazole 8,8-dioxide (1) (2.04 g, 8.41 mmol) was pyrolyzed under vacuum (150 mTorr) at 180 °C in a water-cooled sublimation apparatus overnight. The resulting solids were collected and resublimed under vacuum (150 mTorr) at 180 °C overnight to give the product as a pure yellow solid (1.36 g, 90.6% yield).

^{1}H NMR ($CDCl_3$, 499.74 MHz): δ 8.18 (d, J = 8.4 Hz, 2H), 8.13 (d, J = 8.4 Hz, 2H), 7.68 (t, J = 7.6 Hz, 2H). ^{13}C NMR ($CDCl_3$, 125.67 MHz): δ 138.00, 134.68, 133.55, 128.99, 126.84,

116.81, 109.05. IR (neat): 3061, 2227, 2215, 1586, 1571, 1512, 1372, 1360, 1230, 1218, 1174, 1111, 1092, 990, 970, 943, 828, 779, 761, 694, 666 cm^{-1}. HR-DART/MS (m/z): $[M+H]^+$ 179.0605 (found); $C_{12}H_7N_2$ 179.0609 (calcd).

Synthesis of 1,8-naphthalimide dioxime, 3, (Np-CAO-H3)

Hydroxylamine hydrochloride (0.982 g, 14.1 mmol) and potassium hydroxide (0.793 g, 14.1 mmol) were added to 1,8-dicyanonaphthalene (0.504 g, 2.83 mmol) in water (18 mL) and ethanol (6 mL). The reaction mixture was stirred at 80 °C overnight and then cooled to room temperature, filtered, and washed with cold ethanol. The solid residue was recrystallized from boiling absolute ethanol (50 mL) and dried under vacuum for 1 h to give the product as yellow needles (0.351 g, 54.6% yield). The product was stored under nitrogen to prevent oxidation that occurs over a 4 d period to form the dark red-brown 1,8-naphthalimide.

^{1}H NMR (DMSO-d_6, 499.74 MHz): δ 11.05 (s, 2H), 8.96 (s, 1H), 8.14 (d, J = 7.0 Hz, 2H), 8.06 (d, J = 7.9 Hz, 2H), 7.63 (t, J = 7.6 Hz, 2H). ^{13}C NMR (DMSO-d_6, 125.67 MHz): δ 141.02, 132.40, 129.42, 126.40, 125.66, 121.90, 120.59. ^{13}C SSNMR (Adamantane standard, 100.53 MHz): δ 144.65, 130.84, 127.05, 125.19, 120.97. ^{13}C SSNMR (interrupted decoupling, Adamantane standard, 100.53 MHz): δ 144.82, 131.16, 125.33, 120.95. IR (neat): 3407, 3384, 3058, 2813, 1642, 1606, 1469, 1433, 1387, 1332, 1217, 1165, 1085, 1003, 957, 898, 872, 827, 794, 764, 719, 685, 667, 641, 610 cm^{-1}. HR-DART/ MS (m/z): $[M+H]^+$ 228.0773 (found); $C_{12}H_{10}N_3O_2$ 228.0773 (calcd).

Synthesis of (Np-CAO-H_2)U(O)$_2$(NO_3)(CH_3OH), 4

A solution of 1,8-naphthalimide dioxime (0.0386 g, 0.170 mmol) in methanol (19 mL) was added to a solution of uranyl nitrate hexahydrate (0.0873 g, 0.173 mmol) in methanol (19

mL). The complex was formed and crystallized by slow evaporation from the methanol solution after 2 d. The remaining solution was decanted, and the red crystals were washed once with methanol before air drying (0.0453 g, 45.2% yield). ^{13}C SSNMR (Adamantane, 100.53): δ 151.92, 132.52, 127.97, 114.68. ^{13}C SSNMR (interrupted decoupling, Adamantane, 100.53): δ 151.73, 132.03, 125.32, 114.24. IR (neat): 3307, 2915, 1627, 1596, 1512, 1370, 1341, 1287, 1238, 1223, 1170, 1108, 1055, 1040, 1008, 910, 836, 808, 796, 770, 750, 705, 688 cm^{-1}. HR-ESI/MS (m/z): $[M\text{-}NO_3\text{-}CH_3OH+2DMSO]^+$ 652.1269, $[M\text{-}NO_3\text{-}CH_3OH+DMSO]^+$ 574.1144, $[M\text{-}NO_3\text{-}CH_3OH]^+$ 496.1042 (found); $[M\text{-}NO_3\text{-}CH_3OH+2DMSO]^+$ 652.1301, $[M\text{-}NO_3\text{-}$CH3OH+DMSO]+ 574.1162, $[M\text{-}NO_3\text{-}CH_3OH]^+$ 496.1023 (calcd). Anal. Calc. for $C_{13}H_{12}N_4O_8U$: C, 26.45; H, 2.05; N, 9.49. Found: C, 25.32; H, 1.71; N, 9.62%.

Results and discussion

Synthesis of ligand and uranyl complex

We exploited a three-step strategy to prepare the conjugated cyclic imide dioxime ligand. We synthesized acenaphtho[1,2-c][1,2,5]thiadiazole 8,8-dioxide, **1**, via an acid-catalyzed condensation reaction with sulfamide in refluxing ethanol that was modified from Qian (Scheme 1) [19]. Following a modification of Ege's synthesis [21], compound **1** was subjected to pyrolysis under dynamic vacuum (150 mTorr) at 180 °C which caused the loss of sulfur dioxide and formation of 1,8-dicyanonaphthalene, **2**. The loss of sulfur dioxide to form aromatic dinitriles has previously been reported by Ege and Hay [21,36]. Following the method of Forrester, 1,8-dicyanonaphthalene reacted with hydroxylamine in a refluxing ethanol and water mixture to form 1,8-naphthalimide dioxime, **3**, (Np-CAO-H_3) [22]. The ligand (**3**) can be

purified by crystallization from absolute ethanol and must be stored under nitrogen to prevent slow decomposition. Compounds **1**–**3** were characterized by ^{1}H and ^{13}C NMR as well as HR-DART/MS and IR. The uranyl complex, (Np-CAO-H_2)U$(O)_2(NO_3)(CH_3OH)$, **4**, was prepared by mixing **3** and uranyl nitrate hexahydrate in methanol (Scheme 1). Red crystals of **4** that were suitable for single crystal diffraction were formed in 45% yield after 2 days. Single crystal diffraction demonstrated that the uranyl center is coordinated to a single cyclic dioxime ligand, a bidentate nitrate group, and a methanol in the equatorial plane. This result is in contrast to the unconjugated cyclic imide dioxime ligand prepared by Rao wherein two equivalents bind to the metal center. Even addition of excess **3** still yielded **4** and not the bis tridentate amidoxime uranyl product (Np-CAO-$H_2)_2$U$(O)_2$. X-ray diffraction shows that the geometry about the uranium atom can best be described as hexagonal bipyramidal (Fig. 1) [37–39]. Each atom that is ligated to the uranium has a respectively ligated atom that is nearly *trans* to it. The two oxo ligands are bound in the axial positions and show only a mild distortion of the O_1-U-O_2 bond angle of 177.1°. The U-O bond distances are asymmetric (U-O_1, 1.781(6); U-O_2, 1.767(6)) and are well within the range of similar uranyl complexes [40–42]. Like Rao's glutarimidedioxime uranyl complex, central nitrogen (N_4) is deprotonated and a proton shift occurs on the oxime groups creating an extended aromatic structure [15]. The U-N_4 bond distance for **4** is 2.514(1) Å, which is slightly shorter than the UAN bond distance (2.563(3) Å) found in Rao's glutarimidedioxime uranyl complex [15]. This chelating imide dioxime is a rare example of tridentate binding to uranyl with this class of ligands [15], and contrasts to the binding motif of amidoximates to uranyl [33].

Spectroscopic characterization of uranyl complex

Although a few similar uranyl imide dioxime complexes have been prepared previously by Rao and others, almost no detailed spectroscopic work has been undertaken outside of UV–

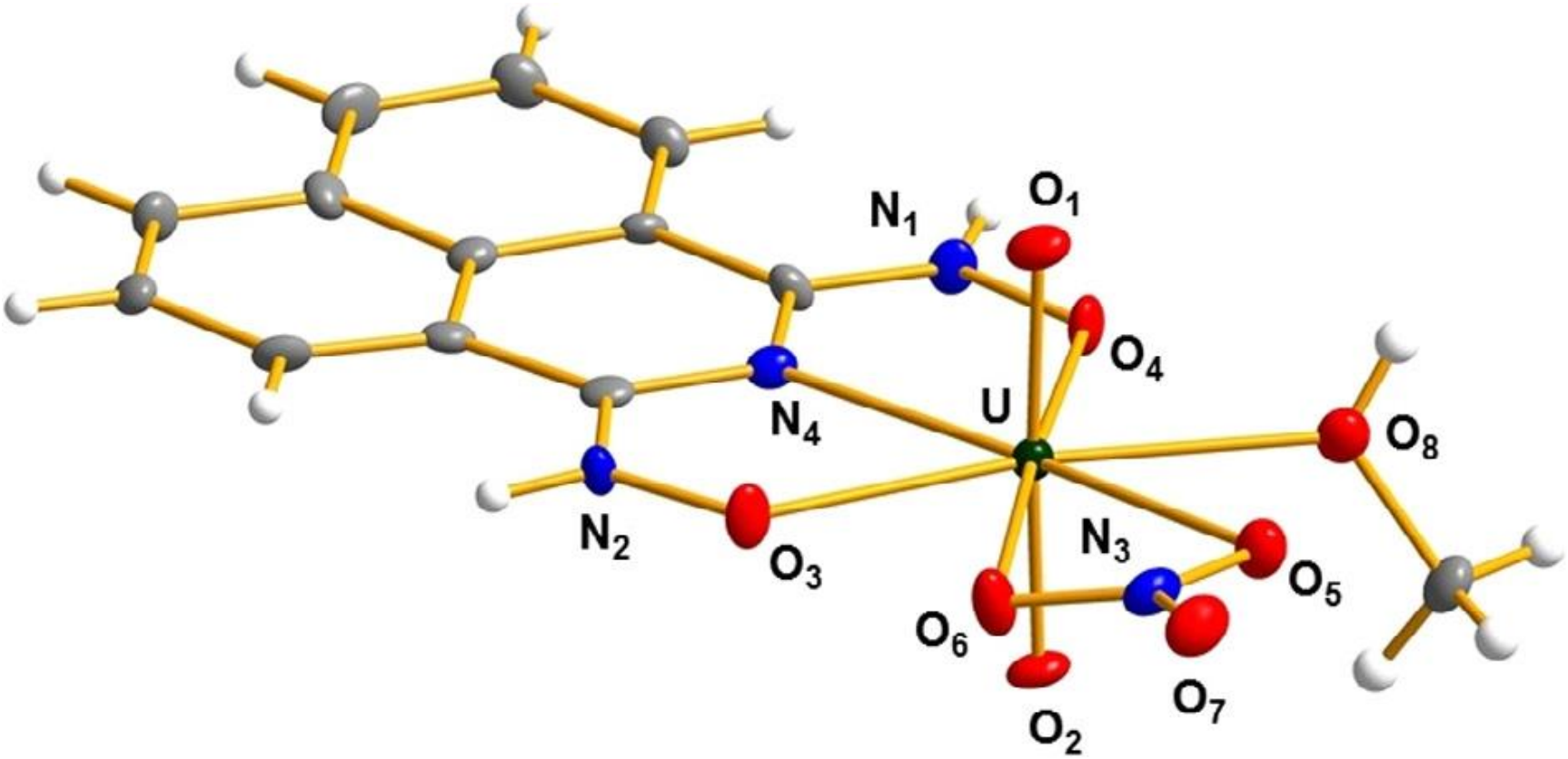

Fig. 1. Crystal structure of (Np-CAO-H_2)U($O)_2$(NO_3)(CH_3OH) (**4**) that shows tridentate binding of cyclic amidoxime ligand. Green, blue, red, and gray ellipsoids (50% probability) represent U, N, O, and C, respectively. White spheres represent H. Selected bond distances (Å) and angles (°) are as follows: U-O_1, 1.781(6); U-O_2, 1.767(6); U-O_3, 2.398(6); U-O_4, 2.420(6); U-O_5, 2.589(6); U-O_6, 2.572(6); U-O_8, 2.462(7); U-N_4, 2.514(7); O_1-U-O_2, 177.1(3); O_3-U-O_8, 170.1(2); O_4-U-O_6, 176.8(2); O_5-U-N_4, 169.0(2).

Vis measurements [15–17]. Detailed NMR spectroscopy has not been collected for uranyl imide dioxime complexes and provides an effective method for determination of uranyl complexation. One area that would also be of potential importance for nuclear forensics is a detailed understanding of the vibrational spectroscopy associated with binding ligands such as imide dioximes and the specific actinides targeted.

Since uranyl complex **4** has very low solubility in common organic solvents, we employed solid state ^{13}C CP MAS NMR. To unambiguously determine the peak positions for each carbon, solution state ^{1}H and ^{13}C NMR, along with HSQC and HMBC spectra, were collected for ligand **3** in DMSO-d_6 (SI Figs. S1 and S2). These solution spectra were compared to a ^{13}C CP MAS NMR spectrum of **3** (SI Fig. S3), but the width of the peaks in the ^{13}C CP MAS NMR spectrum made assignment of each individual carbon signal problematic.

To simplify the assignment of the peak positions, in particular the imine carbon as it is the closest in proximity to the bound uranyl in **4**, we turned to interrupted decoupling NMR. Interrupted decoupling serves to suppress protonated carbons, therefore removing a majority of the aromatic carbons and allowing for assignment of the individual carbon atoms of interest [43,44]. When the protonated carbons were suppressed, four clearly resolved resonances at 121.0, 125.3, 131.2, and 144.8 ppm were observed (Fig. 2A). An interrupted decoupling NMR was then collected for complex **4** as standard ^{13}C CP MAS NMR again led to broad, unassignable peaks (SI Fig. 3B) and showed four resonances at 114.7, 128.0, 132.5, and 151.9 ppm. The imine carbon (denoted ‘‘a’’ in Fig. 2) resonance shifts significantly downfield by 7.1 ppm as the carbons are deshielded compared to the free ligand, providing evidence that the ligand is now bound [38]. Solid state ^{13}C CP MAS NMR has rarely been employed on uranyl complexes and, to our knowledge, interrupted decoupling ^{13}C CP MAS NMR has never been

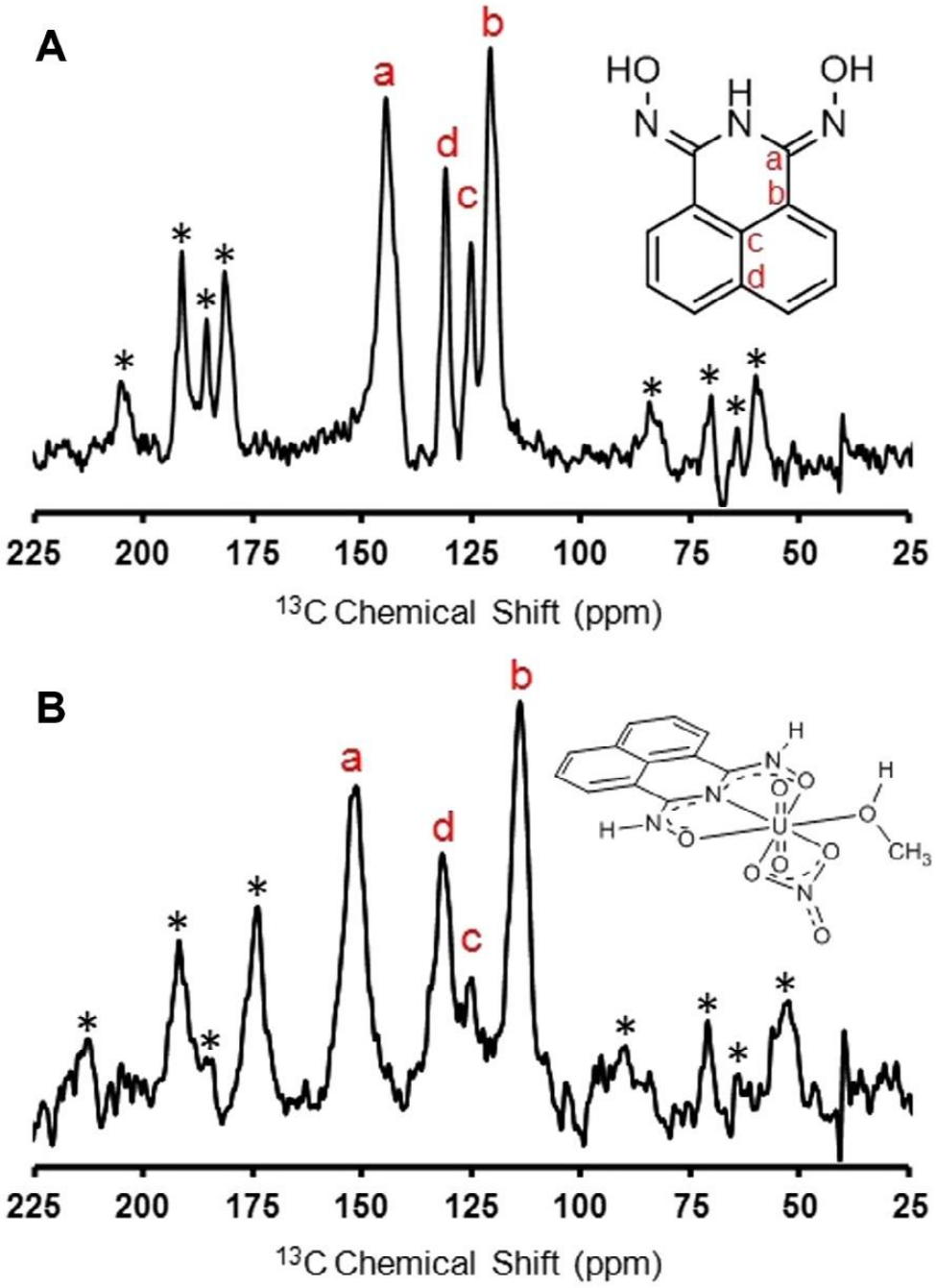

Fig. 2. (A) The ^{13}C CP MAS NMR of **3** with interrupted decoupling exhibiting the resonances of the four quaternary carbons. (B) The ^{13}C CP MAS NMR of **4** with interrupted decoupling revealing the shifted resonances of the four quaternary carbons in the ligand. *Denote spinning sidebands.

performed [42]. This solid state spectroscopic method is an effective technique that demonstrates that the ligand is bound to the uranyl in the bulk material.

While NMR may not be effective for nuclear forensics due to lack of portability, vibrational spectroscopy of uranyl complexes may be more insightful for field-based tests. The vibrational spectroscopy of uranyl species, $UO_2(NO_3)_2 \cdot 6H_2O$ in particular, have been previously characterized [45–48,9], and our results are in agreement with these previous studies. The IR spectrum of the uranyl nitrate hexahydrate is dominated by the intense and broad asymmetric uranyl ($\nu_{U=O,as}$) stretch at 935 cm^{-1}, while a weak symmetric uranyl ($\nu_{U=O,s}$) stretch is visible at 867 cm^{-1}. The ligand **3** exhibits characteristic imide and oxime vibrations with the ν_{O-H} stretch at 3407 cm^{-1}, ν_{N-H} stretch at 3384 cm^{-1}, $\nu_{N=C}$ stretch at 1642 cm^{-1}, and ν_{N-O} stretch at 957 cm^{-1}. Upon mixing the ligand–UO_2 complex **4**, it exhibits a combination of stretches from the ligand, UO_2, and NO_3, moieties. Of special note is the shifting of peaks in the uranyl region (~1000–800 cm^{-1}) as shown in Fig. 3. All of the characteristic vibrations from the UO_2 and ligand **3** in this region have shifted from their original positions.

The Raman spectrum of the uranyl salt is dominated by the $\nu_{U=O,s}$ stretch at 867 cm^{-1} while the $\nu_{U=O,as}$ stretch is virtually indistinguishable from noise. The Raman spectrum of the ligand **3** exhibits a small fluorescence background even after purification by recrystallization, although this is not unexpected from a conjugated system. The Raman spectrum is characterized by an intense mode at 1380 cm^{-1} and a weaker feature at 511 cm^{-1}. Upon binding, the large polarizability of the UO_2 group results in the spectra of the complex **4** being dominated by the $\nu_{U=O,s}$ stretch. However, as mentioned previously[46,48,49], the $\nu_{U=O,as}$ stretch at 918 cm^{-1} is forbidden in the Raman spectrum and is practically unnoticeable. In the Raman spectrum the

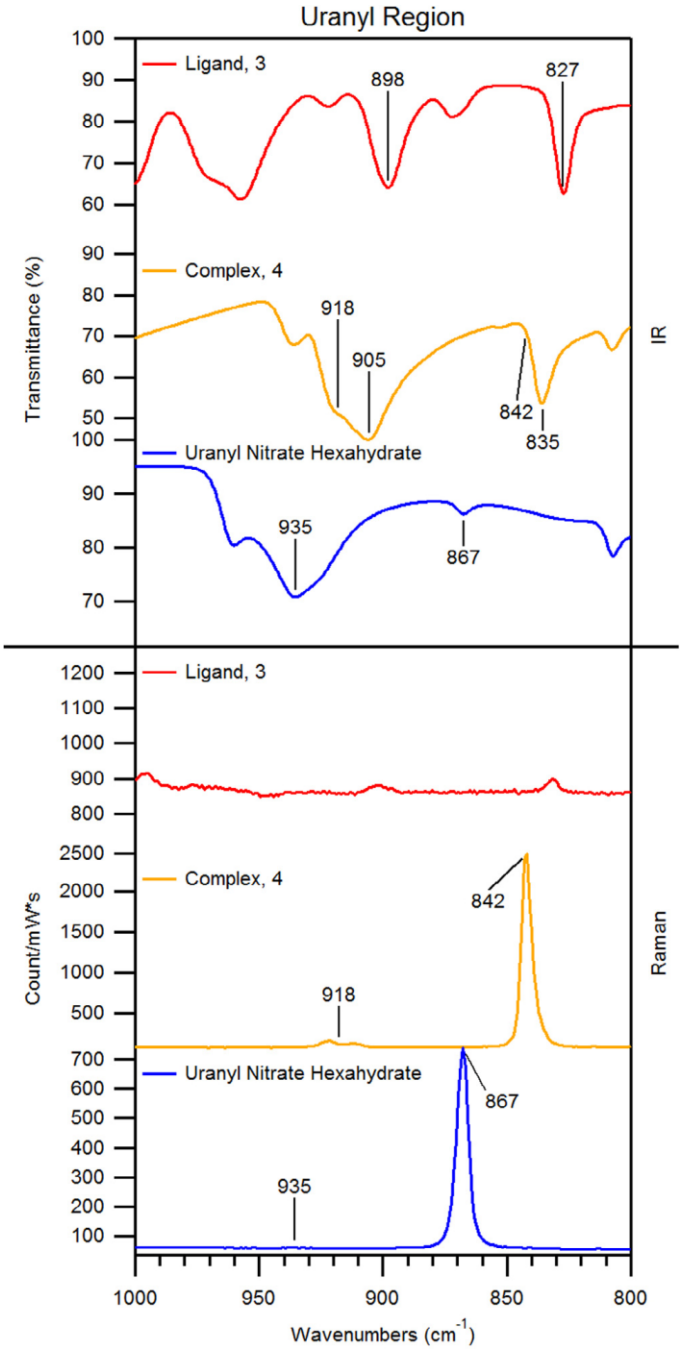

Fig. 3. The uranyl region ($U(O)_2$) of the vibrational spectra, both IR (top) and Raman (bottom). The spectra of ligand **3**, complex **4**, and uranyl nitrate hexahydrate are shown from top to bottom. The positions, left to right, of the antisymmetric (ν_{as}) and symmetric (ν_s) U=O stretches are labeled for uranyl and the complex while competing vibrations are labeled for the ligand.

$\nu_{U=O,s}$ stretch is free of competing ligand vibrations, has a very strong intensity and is distinct. Thus the frequency of the stretch can serve as a clear indicator for the complexation of uranyl.

Due to the expansive, vibration free region around the $\nu_{U=O,s}$ stretch it is likely that the symmetric stretch from other actinides would also be clearly visible with this ligand system. Many theoretical and experimental studies have demonstrated the sequential trend of the $\nu_{An=O,s}$ and $\nu_{An=O,as}$ stretching frequencies of uranium, neptunium, and plutonium oxycation moities [50–53]. We believe the sparseness of the uranyl region in the Raman spectra coupled with the sequential nature of the actinide oxycations vibrational modes presents an excellent opportunity to use ligand **3** as a detection sensor for the associated hexavalent actinide cations.

Density functional theory (DFT) calculations of vibrational modes aided in the understanding of changes between the individual molecular systems and the combined complex **4**. In particular it was noted that the $\nu_{U=O,s}$ stretch at 867 cm^{-1} is barely discernible in the IR of the uranyl complex. Once bound, the $\nu_{U=O,s}$ band is blue-shifted to 842 cm^{-1} and overwhelmed by an intense ligand **3** vibration at 835 cm^{-1}. The $\nu_{U=O,as}$ stretch at 935 cm^{-1} is clearly visible in the uranyl complex, though upon binding the uranyl mode is again blue-shifted and a competing vibration from the ligand **3** at 905 cm^{-1} again overwhelms and merges with the uranyl vibration. In both cases the U=O stretch in the IR spectrum is obscured either partially or completely by modes in the ligand **3**. The Raman spectrum of the uranyl salt lacks the $\nu_{U=O,as}$ stretch but clearly shows the $\nu_{U=O,s}$ stretch at 867 cm^{-1} that is shifted to 842 cm^{-1} in the complex. This stretch in the complex **4** is free from significant competing vibrations down to 800 cm^{-1} and up to 910 cm^{-1} which allows for it to be quickly and easily identified unlike either of the uranyl modes in the IR.

Overall, the shifting of the frequencies in the uranyl region can be explained by the expansion of the conjugated system in the ligand to include the uranyl moiety. Further experimental evidence is presented in the bond lengths between uranium and the oxo ligands. The uranyl group in the uranyl nitrate has bond lengths of 1.770 and 1.749 Å while the group in the complex (**4**) has bond lengths of 1.781 and 1.767 Å, respectively [54]. The inclusion of the uranyl moiety in the conjugated system leads to loss of electron density between the uranium and oxo ligands. This weakens the bonds, leading to elongated bond lengths.

DFT studies of uranyl complex

DFT calculations of the uranyl complex were performed to gain a greater understanding of the electronic structure of the system. Electronic orbital modeling of uranyl systems has been discussed previously [55–63]. The geometry-optimized structure was compared with the crystal structure and generally found to be in good agreement given the comparison of gas and crystal phase results (e.g., all U-O distances agreed within 0.08 Å except to the methanol oxygen which was 0.13 Å shorter in the computation). Upon binding, one significant change in the ligand geometry was a shortening by approximately ~0.09 Å of the O3-N2 and N1-O4 distances in the optimized structure of **4** compared to the experimentally determined structure. This bond shortening suggests delocalized electron density on the O-N-C-N-C-N-O ligand backbone, which could substantiate the notion of a highly conjugated system. These results were consistent with Rao's finding for a uranyl complexed to glutarimidedioxime [15]. In addition, the ligand–U bond lengths were all within 0.10 Å of the experimentally determined structures except for the bound methanol (O8), which was 0.13 Å further from uranium in the calculated structure. Overall, the accurate reproduction of the experimental complex gives us confidence that our electronic structure methods are valid.

The molecular orbitals around the HOMO and LUMO are, naturally, of special interest. When examining the highest occupied molecular orbital (HOMO) (Fig. 4b) and adjacent lower orbitals, the majority of contributions come from ligand-based p-orbitals (Fig. S5). In the case of the lowest unoccupied molecular orbital (LUMO) (Fig. 4a), most of the electron density is also ligand based, with a small contribution (10%) from an f-orbital. This result is in contrast with the LUMO+1 to LUMO+4 orbitals that show exclusively f-orbital character (Fig. S6). Finally, we note that the complex 4 has a reasonably large HOMO–LUMO gap of approximately 61.24 kcal/mol.

Conclusion

In summary, we present a comprehensive synthetic, spectroscopic, and theoretical characterization of an aromatic tridentate amidoxime uranyl complex. The X-ray structure of the complex demonstrates that unlike Rao's tridentate amidoxime complex, only one equivalent of this aromatic ligand binds to the uranyl ion. The solid state NMR spectrum of the complex is, to our knowledge, the first NMR taken of a combined amidoxime-uranium complex and demonstrates complexation of the bulk material. DFT afforded insight into the electronic structure of this uranyl complex as well as assisted in assigning the vibrational modes. While the U=O vibrations were obscured in the IR spectrum by nearby vibrations, they were easily observed in the Raman spectrum and these signals in the Raman spectra could potentially serve as a spectroscopic marker for uranium detection. The thorough evaluation of this complex's vibrational spectra is a critical first step in the development of cyclic polydentate amidoximes for nuclear forensics and may also aid in situ investigations of extraction of uranyl from seawater.

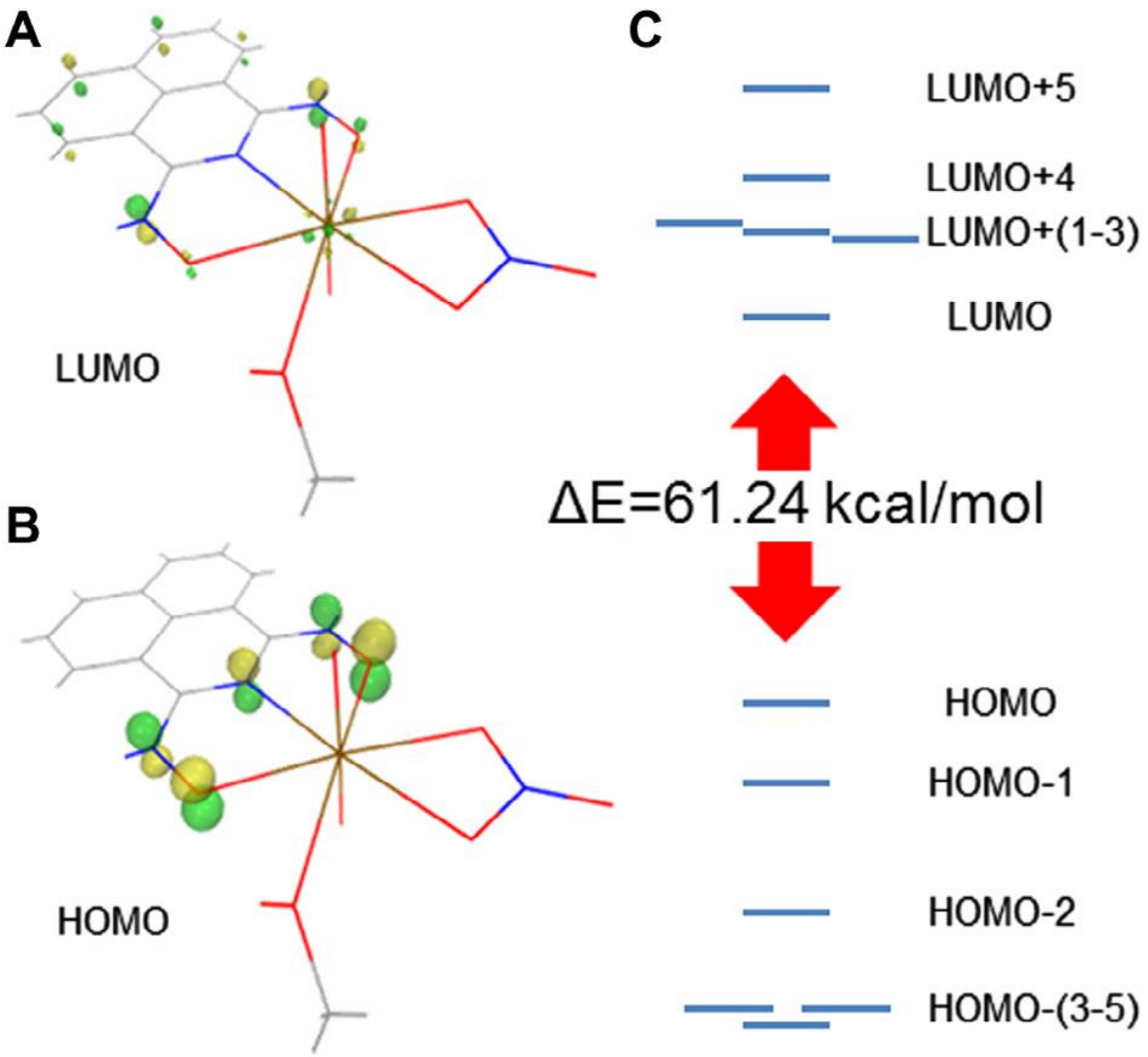

Fig. 4. (A) LUMO of (Np-CAO-H_2)U$(O)_2(NO_3)(CH_3OH)$ (**4**). (B) HOMO of complex **4**. (C) Orbital splitting diagram of complex **4** obtained from DFT calculations. All calculations used NWChem/B3LYP/6-311++g**

References for Chapter II

[1] K. Mayer, M. Wallenius, Z. Varga, Chem. Rev. 113 (2012) 884.

[2] M.J. Kristo, S.J. Tumey, Nucl. Instrum. Methods Phys. Res., Sect. B 294 (2013) 656.

[3] H. Sodaye, S. Nisan, C. Poletiko, S. Prabhakar, P.K. Tewari, Desalination 235 (2009) 9.

[4] P.S. Barber, S.P. Kelley, C.S. Griggs, S. Wallace, R.D. Rogers, Green Chem. 2014 (1828) 16.

[5] H.J. Schenk, L. Astheimer, E.G. Witte, K. Schwochau, Sep. Sci. Technol. 17 (1982) 1293.

[6] J. Kim, C. Tsouris, R.T. Mayes, Y. Oyola, T. Saito, C.J. Janke, S. Dai, E. Schneider, D. Sachde, Sep. Sci. Technol. 48 (2013) 367.

[7] R.V. Davies, J. Kennedy, K.M. Hill, R.W. McIlroy, R. Spence, Nature 203 (1964) 1110.

[8] M.J. Tamada, Jpn. Inst. Energy 88 (2009) 249.

[9] D. Bhandari, S.M. Wells, S.T. Retterer, M. Sepaniak, J. Anal. Chem. 81 (2009) 8061.

[10] L. Astheimer, H.J. Schenk, E.G. Witte, K. Schwochau, Sep. Sci. Technol. 18 (1983) 307.

[11] A. Zhang, G. Uchiyama, T. Asakura, Adsorp. Sci. Technol. 21 (2003) 761.

[12] A. Zhang, T. Asakura, G. Uchiyama, React. Funct. Polym. 57 (2003) 67.

[13] A. Zhang, G. Uchiyama, T. Asakura, Sep. Sci. Technol. 2003 (1829) 38.

[14] B.P. Hay, O. Clement, G. Sandrone, D.A. Dixon, Inorg. Chem. 37 (1998) 5887.

[15] G.X. Tian, S.J. Teat, Z.Y. Zhang, L.F. Rao, Dalton Trans. 41 (2012) 11579.

[16] X. Sun, G. Tian, C. Xu, L. Rao, S. Vukovic, S.O. Kang, B.P. Hay, Dalton Trans. 43 (2014) 551.

[17] G.X. Tian, S.J. Teat, L.F. Rao, Dalton Trans. 42 (2013) 5690.

[18] C.L. Bell, C.N.V. Nambury, L. Bauer, J. Org. Chem. 29 (1964) 2873.

[19] X.H. Qian, Y. Xiao, Tetrahedron Lett. 43 (2002) 2991.

[20] J.B. Wright, J. Org. Chem. 1964 (1905) 29.

[21] G. Ege, E. Beisiege, Synthesis (1974) 22.

[22] A.R. Forrester, H. Irikawa, R.H. Thomson, S.O. Woo, T.J. King, J. Chem. Soc., Perkin Trans. 1 (1981) 1712.

[23] Bruker, SAINT-PLUS, Bruker AXS Inc., M., Wisconsin, USA, 2007.

[24] A.L. Spek, PLATON, A Multipurpose Crystallographic Tool, Utrecht University, Utrecht, The Netherlands, 2005.

[25] M. Valiev, E.J. Bylaska, N. Govind, K. Kowalski, T.P. Straatsma, H.J.J. Van Dam, D. Wang, J. Nieplocha, E. Apra, T.L. Windus, W. de Jong, Comput. Phys. Commun. 181 (2010) 1477.

[26] A.D. Becke, J. Chem. Phys. 98 (1993) 5648.

[27] A.D. Becke, Phys. Rev. A 38 (1988) 3098.

[28] C.T. Lee, W.T. Yang, R.G. Parr, Phys. Rev. B 37 (1988) 785.

[29] M. Dolg, H. Stoll, H. Preuss, R.M. Pitzer, J. Phys. Chem. 97 (1993) 5852.

[30] R. Krishnan, J.S. Binkley, R. Seeger, J.A. Pople, J. Chem. Phys. 72 (1980) 650.

[31] D. Feller, J. Comput. Chem. 17 (1996) 1571.

[32] K.L. Schuchardt, B.T. Didier, T. Elsethagen, L.S. Sun, V. Gurumoorthi, J. Chase, J.

Li, T.L. Windus, J. Chem. Inf. Model. 47 (2007) 1045.

[33] S. Vukovic, L.A. Watson, S.O. Kang, R. Custelcean, B.P. Hay, Inorg. Chem. 51 (2012) 3855.

[34] W. Humphrey, A. Dalke, K. Schulten, J. Mol. Graph. 14 (1996) 33.

[35] Persistence of Vision (TM) Raytracer, version 3.7.0, Persistence of Vision Pty. Ltd., Williamstown, Victoria, Australia, 2004.

[36] C.D. Grant, S.O. Kang, B.P. Hay, J. Org. Chem. 78 (2013) 7735.

[37] L.L. Liang, Y.G. Cai, N.S. Weng, R.L. Zhang, J.S. Zhao, J.F. Wang, H.L. Wu, Inorg. Chem. Commun. 12 (2009) 86.

[38] S.B. Deb, S. Kannan, M.G.B. Drew, J. Coord. Chem. 63 (2010) 3620.

[39] P.S. Barber, S.P. Kelley, R.D. Rogers, RSC Adv. 2 (2012) 8526.

[40] G.X. Tian, L.F. Rao, S.J. Teat, G.K. Liu, Chem. Eur. J. 15 (2009) 4172.

[41] S. Kannan, M.A. Moody, C.L. Barnes, P.B. Duval, Inorg. Chem. 47 (2008) 4691.

[42] J. Jiang, M.J. Sarsfield, J.C. Renshaw, F.R. Livens, D. Collison, J.M. Charnock, M. Helliwell, H. Eccles, Inorg. Chem. 41 (2002) 2799.

[43] D.W. Duff, G.E. Maciel, Macromolecules 23 (1990) 4367.

[44] M.V. Luzgin, A.V. Toktarev, V.N. Parmon, A.G. Stepanov, J. Phys. Chem. C 117 (2013) 22867.

[45] C. Nguyen Trung, G.M. Begun, D.A. Palmer, Inorg. Chem. 31 (1992) 5280.

[46] K. Ohwada, Spectrochim. Acta, Part A 35 (1979) 1283.

[47] S.P. Pasilis, A. Blumenfeld, Inorg. Chem. 50 (2011) 8302.

[48] J.I. Bullock, J. Chem. Soc. A (1969) 781.

[49] A.A. Zazhogin, H.D. Lutz, A.I. Komyak, J. Mol. Struct. 482–483 (1999) 189.

[50] C. Madic, G.M. Begun, D.E. Hobart, R.L. Hahn, Inorg. Chem. 1984 (1914) 23.

[51] C. Madic, D.E. Hobart, G.M. Begun, Inorg. Chem. 22 (1983) 1494.

[52] P.J. Hay, R.L. Martin, G. Schreckenbach, J. Phys. Chem. A 104 (2000) 6259.

[53] The Chemistry of the Actinide and Transactinide Elements, 4th ed., 2011.

[54] J.C. Taylor, M.H. Mueller, Acta Crystallogr. 19 (1965) 536.

[55] J. Su, P.D. Dau, Y.H. Qiu, H.T. Liu, C.F. Xu, D.L. Huang, L.S. Wang, J. Li, Inorg. Chem. 52 (2013) 6617.

[56] J.C. Berthet, P. Thuery, J.P. Dognon, D. Guillaneux, M. Ephritikhine, Inorg. Chem. 47 (2008) 6850.

[57] P.D. Dau, J. Su, H.T. Liu, J.B. Liu, D.L. Huang, J. Li, L.S. Wang, Chem. Sci. 3 (2012) 1137.

[58] J. Su, K. Zhang, W.H.E. Schwarz, J. Li, Inorg. Chem. 50 (2011) 2082.

[59] M. Straka, P. Hrobarik, M. Kaupp, J. Am. Chem. Soc. 127 (2005) 2591.

[60] G. Nocton, P. Horeglad, V. Vetere, J. Pecaut, L. Dubois, P. Maldivi, N.M. Edelstein, M. Mazzanti, J. Am. Chem. Soc. 132 (2010) 495.

[61] C.W. Abney, S.B. Liu, W.B. Lin, J. Phys. Chem. A 117 (2013) 11558.

[62] G.M. Lombardo, A.L. Thompson, F.P. Ballistreri, A. Pappalardo, G.T. Sfrazzetto, G.A. Tomaselli, R.M. Toscano, F. Punzo, Dalton Trans. 2012 (1951) 41.

[63] P.F. Weck, E. Kim, B. Masci, P. Thuery, K.R. Czerwinski, Inorg. Chem. 49 (2010) 1465.

Appendix For Chapter II

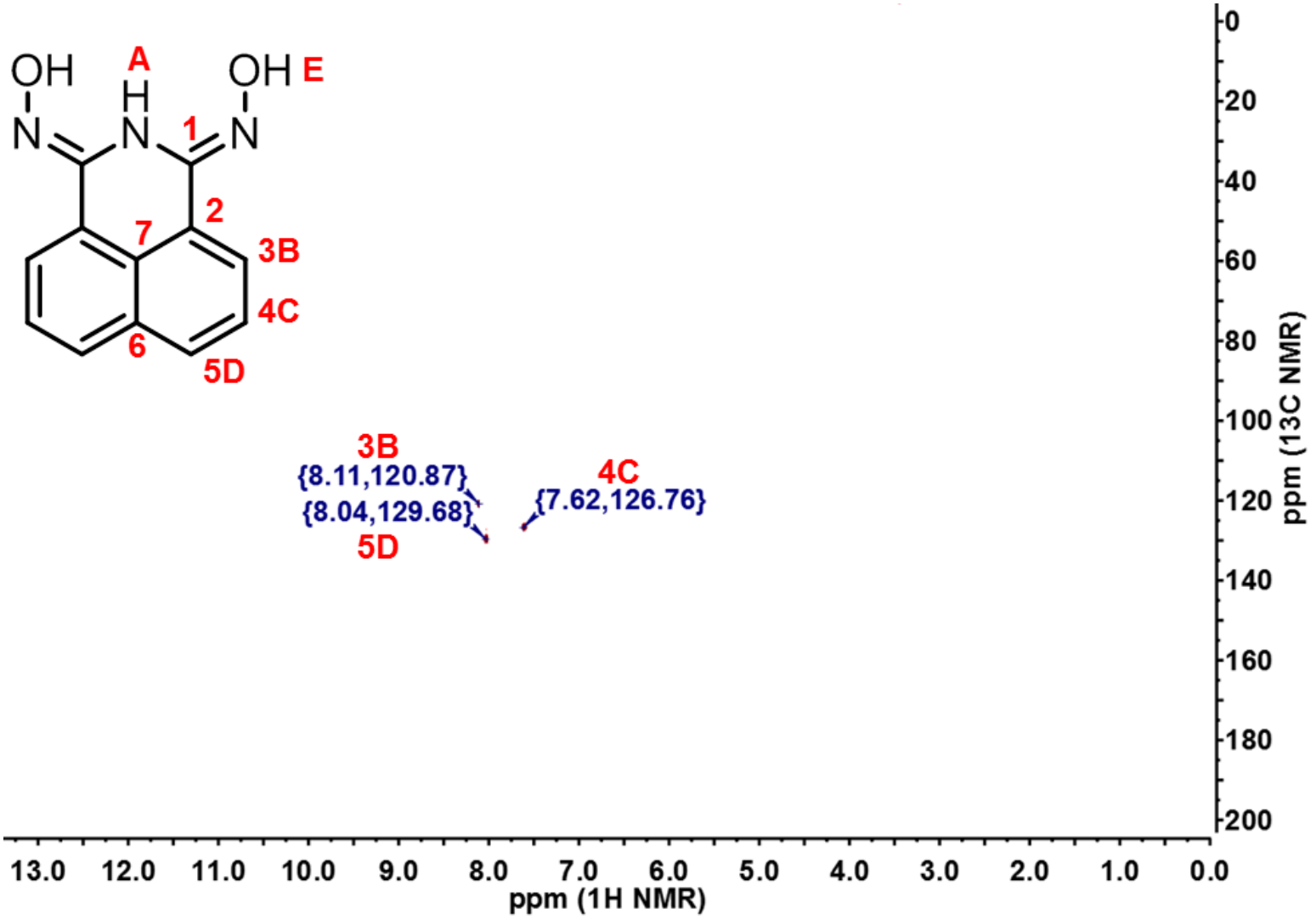

Figure S1. The HSQC NMR spectrum of **3** in DMSO-d_6.

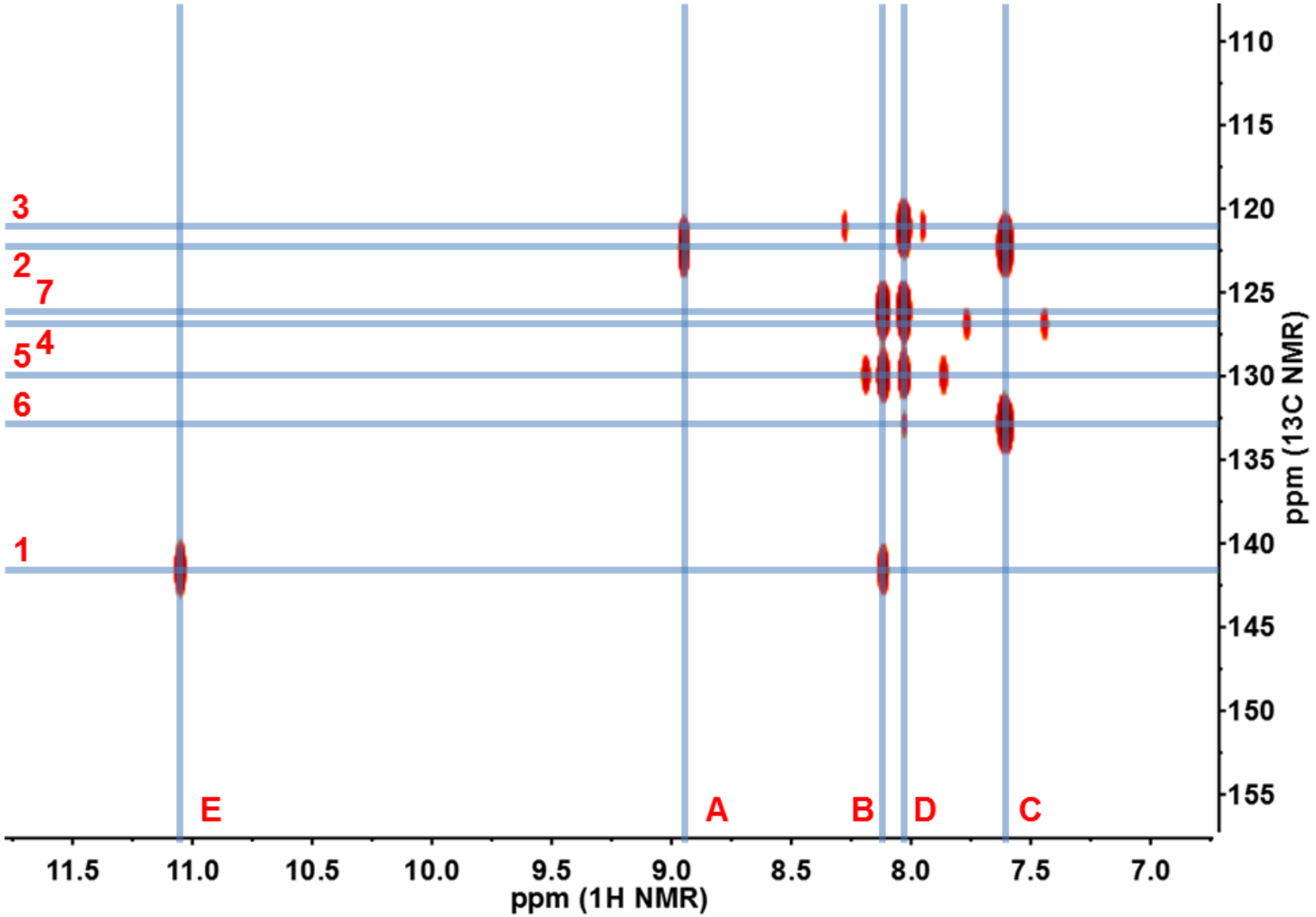

Figure S2. The HMBC NMR spectrum of **3** in DMSO-d_6.

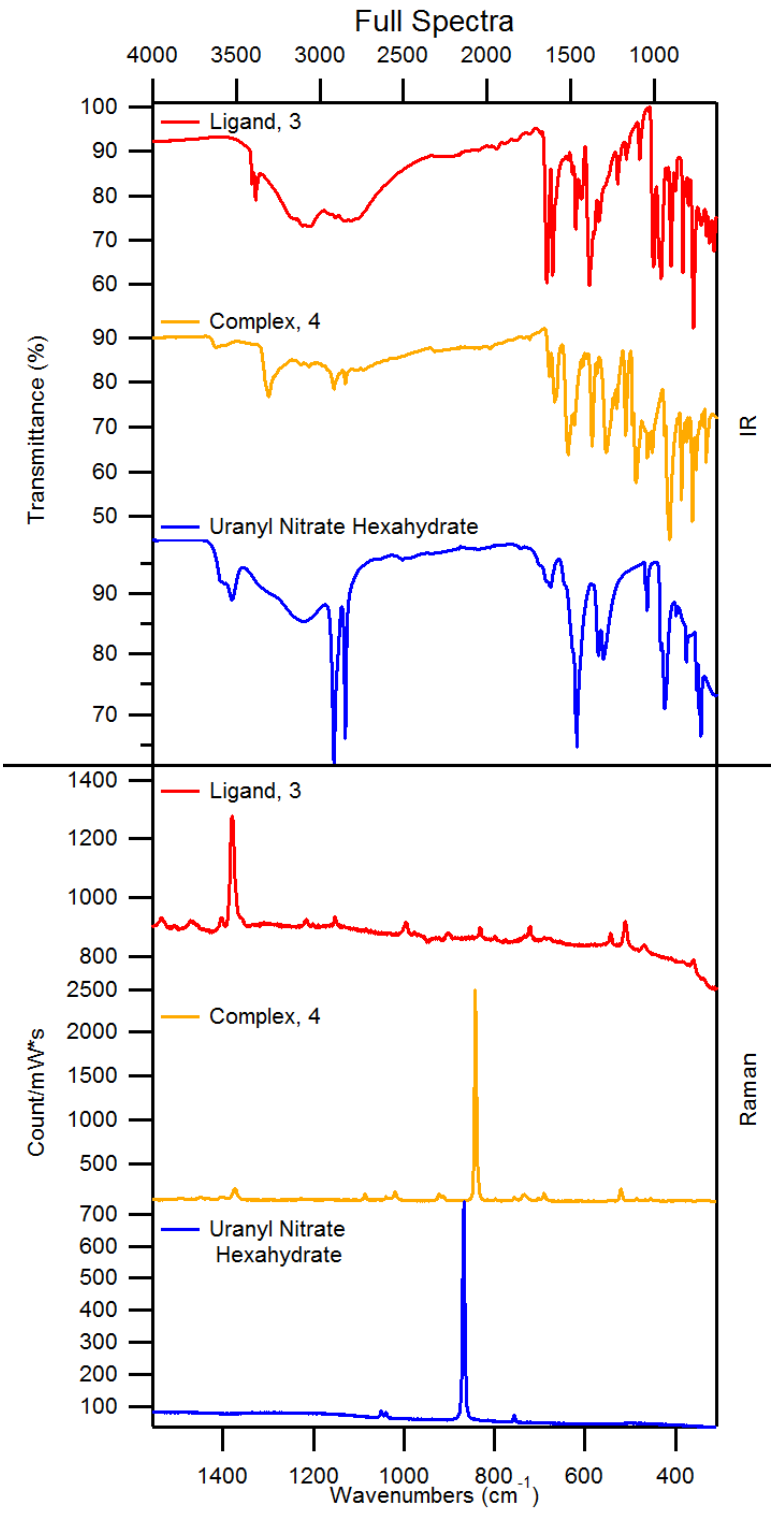

Figure S4. The full Raman and IR spectra of the samples collected.

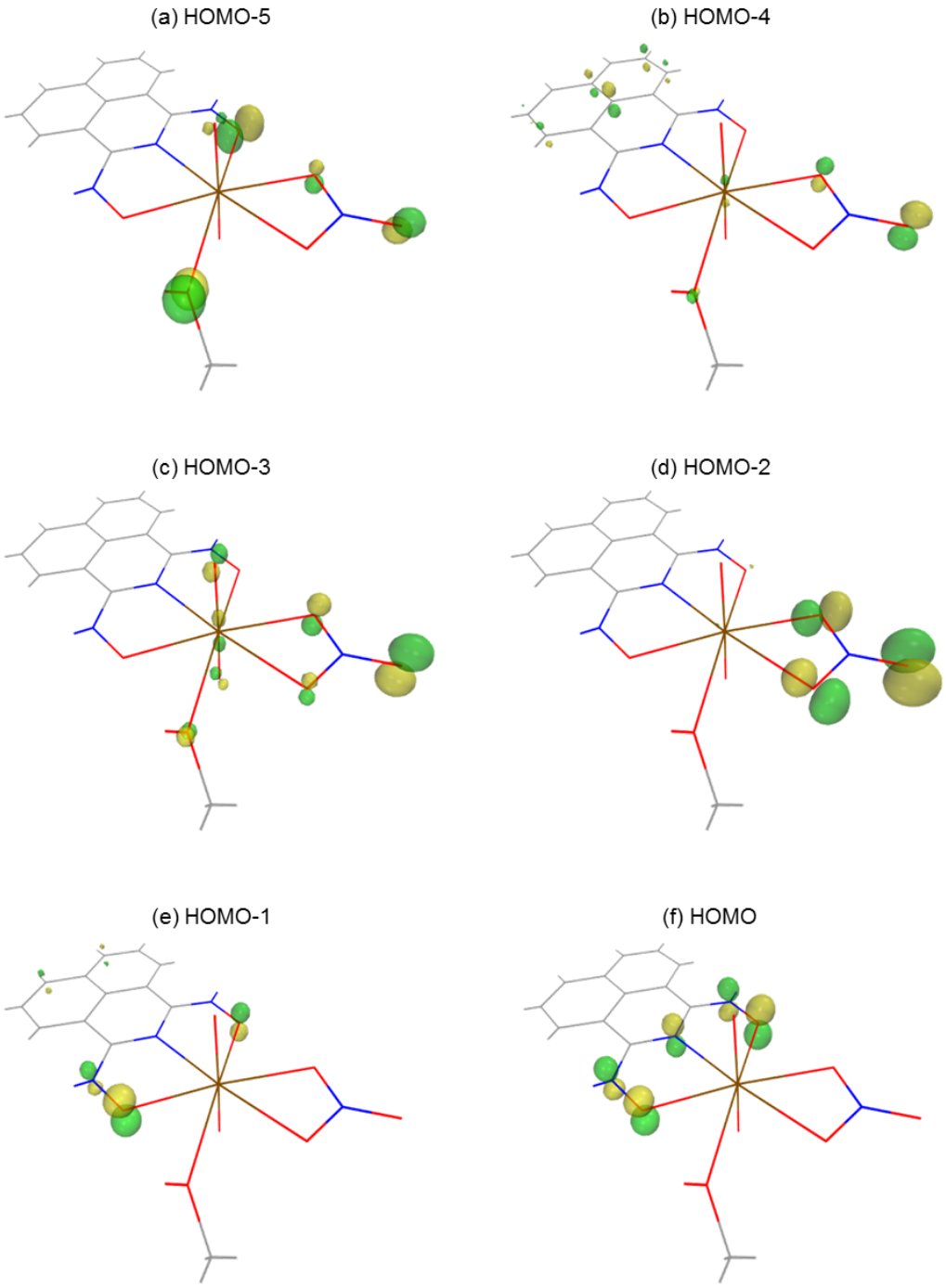

Figure S5. Selected molecular orbital plots from HOMO-5 (a) to HOMO (f).

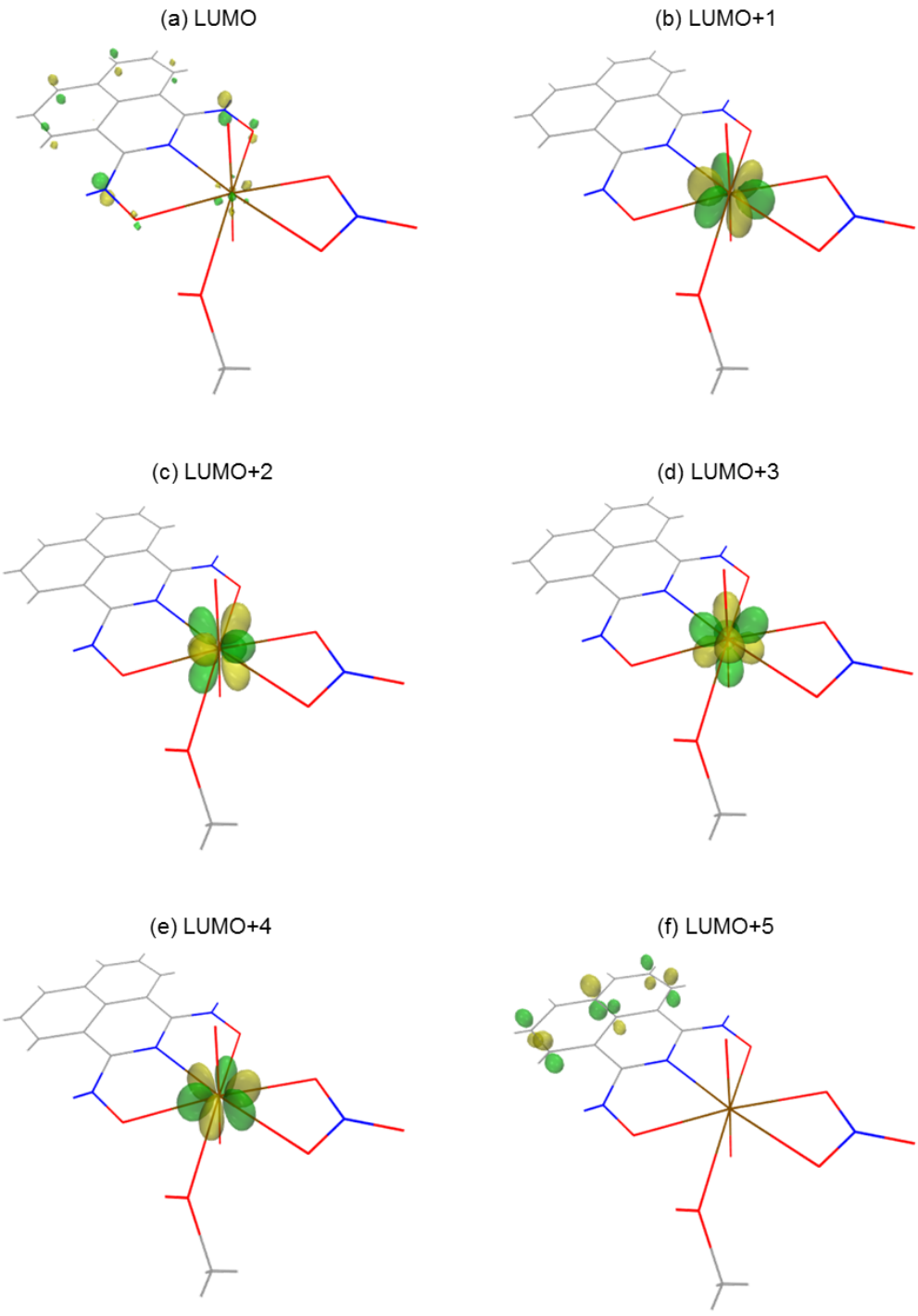

Figure S6. Selected molecular orbital plots from LUMO (a) to LUMO+5 (f).

Vector	Occupancy	E (kcal/mol)	Orbital
113	0	-41.77785877	LUMO+5
112	0	-56.05737593	LUMO+4
111	0	-62.86012399	LUMO+3
110	0	-64.62625088	LUMO+2
109	0	-65.68347973	LUMO+1
108	0	-77.99359441	LUMO
107	2	-139.2314168	HOMO
106	2	-151.9577588	HOMO-1
105	2	-172.4153379	HOMO-2
104	2	-187.5987581	HOMO-3
103	2	-187.7764689	HOMO-4
102	2	-190.3751761	HOMO-5

Table S1. Selected molecular orbital data from HOMO-5 to LUMO+5.

checkCIF/PLATON report

You have not supplied any structure factors. As a result the full set of tests cannot be run.

THIS REPORT IS FOR GUIDANCE ONLY. IF USED AS PART OF A REVIEW PROCEDURE FOR PUBLICATION, IT SHOULD NOT REPLACE THE EXPERTISE OF AN EXPERIENCED CRYSTALLOGRAPHIC REFEREE.

No syntax errors found. CIF dictionary Interpreting this report

Datablock: U

```
Bond precision:  C-C = 0.0127 A          Wavelength=0.71073

Cell:          a=7.1221(15)       b=10.601(2)      c=13.683(3)
               alpha=102.880(2)   beta=99.789(2)   gamma=98.454(2)
Temperature:   100 K

                Calculated                Reported
Volume          973.9(3)                  973.9(4)
Space group     P -1                      P -1
Hall group      -P 1                      ?
Moiety formula  C13 H12 N4 O8 U, 2(C H4 O) ?
Sum formula     C15 H20 N4 O10 U          C15 H20 N4 O10 U
Mr              654.38                    654.38
Dx,g cm-3       2.231                     2.232
Z               2                         2
Mu (mm-1)       8.397                     8.397
F000            620.0                     620.0
F000'           601.18
h,k,lmax        9,14,18                   9,14,18
Nref            5034                      4526
Tmin,Tmax       0.664,0.777               0.679,0.787
Tmin'           0.651

Correction method= MULTI-SCAN

Data completeness= 0.899          Theta(max)= 28.680

R(reflections)= 0.0465( 4098)     wR2(reflections)= 0.1325( 4526)

S = 1.073                 Npar= 289
```

```
The following ALERTS were generated. Each ALERT has the format
      test-name_ALERT_alert-type_alert-level.
Click on the hyperlinks for more details of the test.
```

Figure S7. Page 1 of **4** cif file.

```
Alert level B
PLAT417_ALERT_2_B Short Inter D-H..H-D       H2N    ..  H9O    ..       1.83 Ang.

Alert level C
PLAT342_ALERT_3_C Low Bond Precision on  C-C Bonds ..............     0.0127 Ang.
PLAT417_ALERT_2_C Short Inter D-H..H-D       H8O    ..  H8O    ..       2.12 Ang.

Alert level G
PLAT002_ALERT_2_G Number of Distance or Angle Restraints on AtSite         10
PLAT005_ALERT_5_G No _iucr_refine_instructions_details  in the CIF          ? Do !
PLAT083_ALERT_2_G SHELXL Second Parameter in WGHT Unusually Large.      12.48
PLAT154_ALERT_1_G The su's on the Cell Angles are Equal ..........    0.00200 Deg.
PLAT710_ALERT_4_G Delete 1-2-3 or 2-3-4 Linear Torsion Angle ... #         54
            N2   -O3   -U1   -O8    -166.40  1.10   1.555   1.555   1.555   1.555
PLAT710_ALERT_4_G Delete 1-2-3 or 2-3-4 Linear Torsion Angle ... #         63
            N1   -O4   -U1   -O6    -175.00  4.00   1.555   1.555   1.555   1.555
PLAT710_ALERT_4_G Delete 1-2-3 or 2-3-4 Linear Torsion Angle ... #         67
            C13  -O8   -U1   -O3      57.10  1.50   1.555   1.555   1.555   1.555
PLAT710_ALERT_4_G Delete 1-2-3 or 2-3-4 Linear Torsion Angle ... #         89
            N3   -O6   -U1   -O4       9.00  4.00   1.555   1.555   1.555   1.555
PLAT860_ALERT_3_G Note: Number of Least-Squares Restraints .......          6

   0 ALERT level A = Most likely a serious problem - resolve or explain
   1 ALERT level B = A potentially serious problem, consider carefully
   2 ALERT level C = Check. Ensure it is not caused by an omission or oversight
   9 ALERT level G = General information/check it is not something unexpected

   1 ALERT type 1 CIF construction/syntax error, inconsistent or missing data
   4 ALERT type 2 Indicator that the structure model may be wrong or deficient
   2 ALERT type 3 Indicator that the structure quality may be low
   4 ALERT type 4 Improvement, methodology, query or suggestion
   1 ALERT type 5 Informative message, check
```

Figure S8. Page 2 of **4** cif file.

It is advisable to attempt to resolve as many as possible of the alerts in all categories. Often the minor alerts point to easily fixed oversights, errors and omissions in your CIF or refinement strategy, so attention to these fine details can be worthwhile. In order to resolve some of the more serious problems it may be necessary to carry out additional measurements or structure refinements. However, the purpose of your study may justify the reported deviations and the more serious of these should normally be commented upon in the discussion or experimental section of a paper or in the "special_details" fields of the CIF. checkCIF was carefully designed to identify outliers and unusual parameters, but every test has its limitations and alerts that are not important in a particular case may appear. Conversely, the absence of alerts does not guarantee there are no aspects of the results needing attention. It is up to the individual to critically assess their own results and, if necessary, seek expert advice.

Publication of your CIF in IUCr journals

A basic structural check has been run on your CIF. These basic checks will be run on all CIFs submitted for publication in IUCr journals (*Acta Crystallographica*, *Journal of Applied Crystallography*, *Journal of Synchrotron Radiation*); however, if you intend to submit to *Acta Crystallographica Section C* or *E*, you should make sure that full publication checks are run on the final version of your CIF prior to submission.

Publication of your CIF in other journals

Please refer to the *Notes for Authors* of the relevant journal for any special instructions relating to CIF submission.

PLATON version of 01/06/2013; check.def file version of 24/05/2013

Figure S9 **Page 3 of** 4 **cif file.**

CHAPTER III.

HYPER-RAMAN SCATTERING OF URANYL NITRATE HEXAHYDRATE

Rational for Hyper-Raman Study of Uranyl Nitrate Hexahydrate

Text.

Experimental Challenges

Text.

CONCLUSION

Text.

VITA

Karl J. Bernstein was born on June 1st, 1985. He graduated Andrews University in 2008 having majored in Chemistry, minored in Physics, and accomplished significant studies in engineering, computer science and mathematics. Following graduation he worked at Physics Enterprises, a small company that manufactures Physics based devices for university level teaching and instruction. In 2010 he began his pursuit of a Doctorate of Philosophy at the University of Tennessee Knoxville. He joined the Camden group and pursued studies in Analytical Chemistry. His research focused on new techniques for spectroscopic detection of Uranium via Raman based approaches.